The effect of dendritic spine morphology on synaptic crosstalk

Two multisynapse models, integrating diffusion on curved surfaces

Tamara Kloek

Technische Universiteit Delft

TU Delft Delft University of Technology

Challenge the future

THE EFFECT OF DENDRITIC SPINE MORPHOLOGY ON SYNAPTIC CROSSTALK

TWO MULTISYNAPSE MODELS, INTEGRATING DIFFUSION ON CURVED SURFACES

by

Tamara Kloek

in partial fulfillment of the requirements for the degree of

Master of Science

in Applied Mathematics

at the Delft University of Technology,

to be defended publicly on Thursday December 17, 2015 at 11:00 AM.

Supervisors:	Dr. ir. F. J. Vermolen,	TU Delft;
	Ir. R. P. T. Kusters,	TU Eindhoven;
Thesis committee:	Dr. ir. F. J. Vermolen,	TU Delft;
	Prof. dr. ir. C. Vuik,	TU Delft;
	Dr. ir. J. L. A. Dubbeldam,	TU Delft.

This thesis is confidential and cannot be made public until December 17, 2015.

TU Delft Delft University of Technology

ABSTRACT

Diffusive processes on curved surfaces are highly relevant for cellular processes and are increasingly used to characterize the behavior of proteins in cell membranes. More specifically, neurotransmitter receptors are present on the cell membranes of neurons (nerve cells) and are important for the signal transduction at synapses, which are the specializations through which neurons communicate. The morphology of the cell membrane at these synapses is nontrivial and this shape strongly affects the receptor lateral diffusion process [1].

The typical shape of a single synapse and its impact on the diffusive process have been studied [1, 2]. An open question however, is how this shape affects the crosstalk between multiple synapses connected to the same dendrite. In other words, how does the release of receptors in one synapse influence the concentration in neighboring synapses. To study this we set up two diffusion models that integrate the morphology of multiple synapses.

CONTENTS

1

INTRODUCTION

Signals are transmitted within an animal body through the nervous system. The control of muscles, processing sensory stimuli and regulating cognitive processes are all carried out by the nervous system. At the cellular level, the nervous system consists of a special types of cells, called neurons. Neurons can transmit signals to other neurons through specialized junctions, called synapses. For healthy functioning of the nervous system it is important that the strength of these connections (synaptic strength) can be specifically controlled. Failure of these mechanisms are associated with neurological and neuropsychiatric disorders like schizophrenia, Alzheimer disease, depression and autism [3, 4].

In chemical synapses the transmitting (presynaptic) neuron releases a chemical substance into the synapse, which can bind to a surface receptor present on the cell membrane of the receiving (postsynaptic) cell. An important factor in the synaptic strength is the amount of receptors present on the synaptic cell membrane of the receiving cell. Therefore, controlling the number of receptors at synapses is essential in synaptic transmission [5].

Surface receptors undergo lateral diffusion over the cell membrane. Therefore, receptors initially present at one synapse, can end up in another synapse. This is an instance in which components from one synapse influence the signal transmission in other synapses, a phenomenon that is called *crosstalk*. Crosstalk undermines the ability of the body to specifically control the strength of individual synapses.

The receiving part of the postsynaptic neuron is called a dendritic spine. Spines are protrusions of the membrane of the postsynaptic cell. They have a typical shape consisting of a thin spine neck and a bulbous spine head, as shown in Figure 2.3. The influence of this geometry on the lateral diffusion process of surface receptors has been studied [1, 2].

The aim of this study is to investigate how this nontrivial morphology of dendritic spines influences crosstalk between multiple synapses connected to the same neuron. To this end we set up two models that integrate diffusion on curved surfaces. The first one is an atomistic, particle-based model in which diffusion is seen as particles undergoing Brownian motion, the second one is a continuum-scale model.

In Chapter 2 we explain the biological framework in which dendritic spines are positioned. Our research questions are also presented there. In Chapter 3 we explore existing models for synaptic receptor trafficking and discuss their results. In Chapter 4 we formulate our two new models for receptor trafficking. Chapter 5 elaborates upon the design of test cases that are used to run simulations and in Chapter 6 results of these test cases are presented. Finally, conclusions and a discussion can be found in Chapter 7.

2

DENDRITIC SPINES AND THEIR ROLE IN THE NERVOUS SYSTEM

2.1. THE NERVOUS SYSTEM

The nervous system is the organ system of the body that coordinates both conscious as well as unconscious actions and transmits signals between different parts of the body. In most animal bodies the nervous system consists of two main parts, the central nervous system (CNS) and the peripheral nervous system. The first one consists of the brain and the spinal cord and the latter one connects the central nervous system to every other part of the body.

At the cellular level the nervous system consists of a special type of cells, called neurons or nerve cells. Their structure allows them to transmit signals fast and effectively to other cells. Internally, signals are sent in the form of electrochemical waves along thin fibers of the cell itself. Between different cells these signals are mainly transmitted through specialized junctions called synapses.

2.1.1. NEURONS

Neurons or nerve cells are the cells that constitute the nervous system. They are characterized by a specific composition that allows them to transmit signals from and to every part of the body. Specialized type of neurons are designed to perform a specific task and include:

- *Sensory neurons* are sensitive to input from outside the body like touch, sound, light, smell and other types of external stimuli. After receiving such stimuli they transmit signals to the central nervous system.
- *Motor neurons* are able to directly or indirectly control muscles or glands after receiving input from the central nervous system.
- *Interneurons* connect neurons to other neurons and are mainly found in the central nervous system.

A typical schematic graphic of the structure of two interconnected neurons can be found in Figure 2.1. Neurons are highly specialized in the processing and transmission of signals and this is reflected in their anatomy. A typical neuron possesses a soma, multiple dendrites, an axon and an axon terminal.

- The *soma* is the cell body of the neuron. It contains the nucleus, where most of the cell's genetic material is located. The nucleus of a neuron is involved in processing signals and determining whether a signal is to be transmitted or inhibited.

- *Dendrites* are thin structures that arise from the cell body and often branch multiple times forming a typical dendritic tree. This collection of dendritic protrusions is where the majority of input to the neuron occurs. They receive input from other neurons and propagate the signal to the cell body.
- An *axon* is a structure that arises from the cell body and carries nerve signals away from the soma to other nerve cells or different parts of the nervous system. Whereas a nerve cell has multiple dendrites it typically possesses only one axon. Compared to dendrites an axon can be very long and signals travel the majority of their distance via axons.
- The *axon terminal* is formed when the axon undergoes extensive branching at its end. It contains the synaptic terminals, where neurotransmitter chemicals are released to communicate with target neurons.

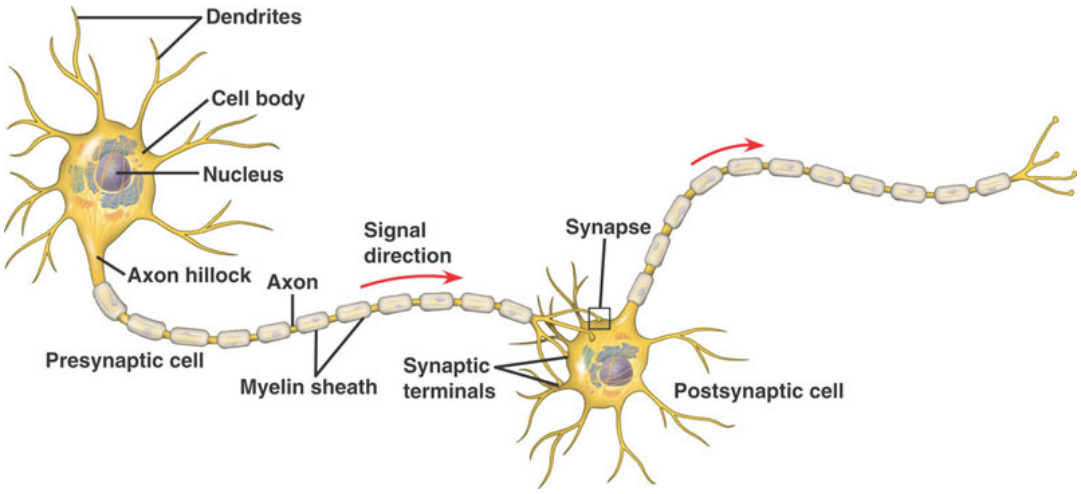

Figure 2.1: Structure of two interconnected neurons. Image: shutterstock.

2.1.2. SYNAPSES

A synapse is a structure where the signal transmission between two neurons occurs. There are two fundamentally different types of synapses: chemical synapses and electrical synapes. In electrical synapses an electronic signal is transmitted by special channels connected to the presynaptic membrane on the one side and to the postsynaptic membrane on the other side.

In this research, we focus on chemical synapses. In chemical synapses the transmitting neuron releases a chemical substance, called neurotransmitter, in the synapse which can bind to a corresponding cell surface receptor on the receiving cell. This cell may then be excited, inhibited or otherwise modulated. Chemical synapses can be subdivided again into two main categories: excitatory and inhibitory synapses. An excitatory synapse is a type of synapse in which an action potential in the presynaptic neuron increases the probability of an action potential occurring in the postsynaptic cell. This is in contrast to inhibitory synapses, which have – as the name suggests – an inhibitory effect on the activation of the postsynaptic neuron. When excitatory effects exceed those of inhibitory effects, the receiving neuron will fire an action potential and thereby information is transferred between the involved neurons. Next, we will focus on excitatory synapses.

ANATOMY AND FUNCTION OF EXCITATORY SYNAPSES

Excitatory synapses have a fundamental role in information processing within the CNS. Knowing the typical anatomy of synapses is crucial in understanding their function. In figure 2.2 a schematic overview of the anatomy of an excitatory synapse is displayed. We discuss the components shown.

In the presynaptic specialization lies a cluster of synaptic vesicles containing neurotransmitter close to the presynaptic cell membrane, which we call the active zone. Exocytosis of these vesicles releases neurotrans-

mitter in the synaptic cleft. An elaborated review of the presynaptic specialization and the synaptic vesicle cycle can be found in [6].

The essential postsynaptic components of an excitatory synapse are located on the dendritic spine, which we discuss in more detail later on. A detailed review of the architecture of the postsynaptic specialization of excitatory synapses can be found in [7]. Opposite the active zone, on the postsynaptic membrane lies its counterpart, a protein dense regime called the postsynaptic density (PSD). The PSD contains scaffold proteins, which are known to interact with neurotransmitter receptors, thus binding them to the PSD [8]. At the PSD neurotransmitter receptors are highly concentrated. The presence of a PSD is characteristic for excitatory synapses, inhibitory synapses lack such a thickening in the postsynaptic cell membrane. The rest of the postsynaptic membrane can be divided into perisynaptic (close to the synapse) and extrasynaptic (outside the synapse) regions. The active zone and the PSD are separated by a gap called the synaptic cleft.

After its release in the synaptic cleft, neurotransmitter binds to and activates a receptor on the postsynaptic membrane. For this reason it is important that enough receptors are present at the site of the PSD in an excitatory synapse. There are many different types of neurotransmitters and corresponding to receptors. Here, we focus mainly on the AMPA and NMDA receptors (AMPAR and NMDAR), because they mediate the majority of rapid excitatory synaptic transmission in the central nervous system [9].

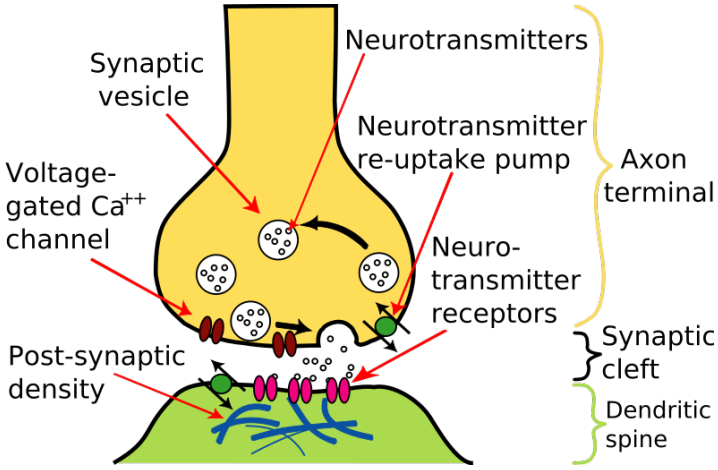

Figure 2.2: Anatomy of an excitatory synapse. CC BY-SA 3.0. Original in [10].

2.1.3. DENDRITIC SPINES

The dendrite of a neuron receives signals from other neurons. Most of the excitatory inputs are located on dendritic spines. Spines are protrusions of the membrane of the postsynaptic cell, on which the PSD is located. They consist of a spine head and a thin spine neck which connects them to the dendritic shaft (figure 2.3). A high correlation is found between the dimensions of spines and the size of the PSD [11, 12]. The shape of spines can be described as “thin”, “filopodia”, “stubby” or “mushroom” (see Fig. 2.4). The dendritic spine is a dynamic structure, whose shape, size and composition change during development and in response to synaptic activity [13, 14]. Changes in their size and shape are connected with a change in synaptic strength [15].

COMPARTMENTALIZATION

The relation between morphology and function is a central theme within biology. The way that the nontrivial morphology of dendritic spines influence their function is not yet fully understood. Having structures like spines containing synapses along the dendrite may have several advantages. Evidently, spines might assist in signaling by physically forming a bridge from axon to dendrite [17]. However, not all synapses are constituted by spines and dendrites can receive inputs directly on their shafts. It is therefore likely that spines are also beneficial in another way. It has been widely suggested that they are associated with *compartmentalization*,

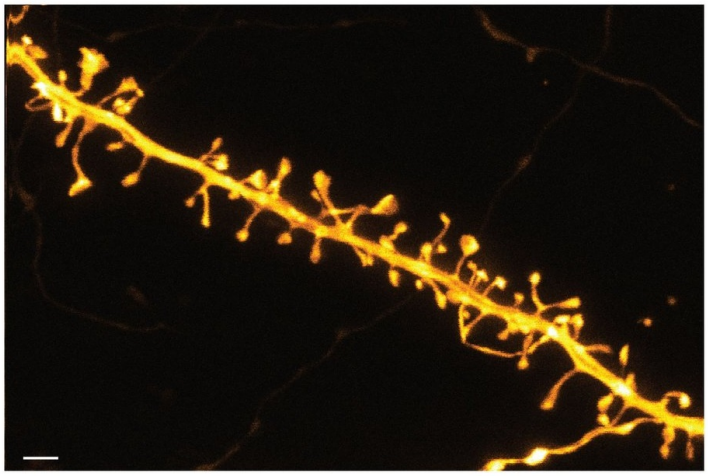

Figure 2.3: STED image recorded from a living dendrite including spines. Source: [16].

enabling synapses to work as independent components [16]. “Mushroom” spines typically have a bulbous head (spine head) and are connected with their corresponding dendrite through a thin spine neck. This morphology has been hypothesized to confine electric signals within the spine head, thereby allowing spines to serve as compartments by which electric signals in one synapse can be isolated from other parts of the neuron [17]. Compartmentalization is essential for the ability of the body to specifically target certain signaling pathways within the (central) nervous system.

2.2. SYNAPTIC PLASTICITY

Synaptic plasticity is the ability of synapses to strengthen and weaken over time, in response to a change in their activity. If this strengthening and weakening persists, then long-lasting increase or decrease in synaptic strength occurs, which is called long-term potentiation (LTP) and long-term depression (LTD) respectively.

Since memories are postulated as networks of neurons in the brain, altering synaptic strength is thought to be one of the most important mechanisms that constitute memory and learning [18]. Synaptic plasticity allows the body to strengthen and weaken certain networks and thereby influencing memories and learning processes. Synaptic transmission of signals and synaptic plasticity are crucial for proper functioning of the central nervous system. Failure of these mechanisms are associated with many neurological and neuropsychiatric disorders like schizophrenia, Alzheimer disease, depression and autism [3, 4]. Furthermore, plasticity of synapses located in the brain (brain plasticity) is thought to play an important role in stroke rehabilitation [19]. Therefore, it is of clinical importance to gain a better understanding of the mechanism that influence synaptic plasticity.

The strength of synaptic transmission between neurons can be modified by various factors, like the density of neurotransmitter receptors located on the postsynaptic neuron [20] and the quantity of neurotransmitters released into the synapse [21]. If the amount of neurotransmitter released into the synapse exceeds a certain threshold in concentration that saturates the postsynaptic receptors, then the number of available and properly functioning receptors will be the most important limiting factor [21, 22]. Controlling the number of receptors at excitatory synapses is of fundamental importance in synaptic transmission [5]. It is therefore of great importance to understand the mechanisms behind receptor trafficking in dendrites and more specifically in dendritic spines.

As mentioned in the previous section, changes in the size and shape of dendritic spines are connected with a change in synaptic strength. Morphological changes that have been reported to accompany LTP include growth of new dendritic spines, elongation of the spine neck, and enlargement of the spine head [15]. The typical characteristics like a long neck and big head develop during LPT, as schematically shown in Figure 2.4.

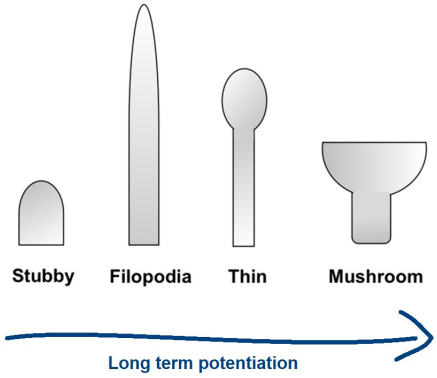

Figure 2.4: Dendritic spine morphologies as reported by [23]. Morphologies develop during long term potentiation as indicated. Figure from [24].

2.2.1. RECEPTOR TRAFFICKING AT SYNAPSES

We know that the phenomena of synaptic plasticity depends strongly on the density of neurotransmitter receptors at the PSD of the postsynaptic cell. Therefore it is interesting to investigate the factors that influence this density. Three main mechanisms that drive the receptor traffic can be distinguished. They are shown in Figure 2.5.

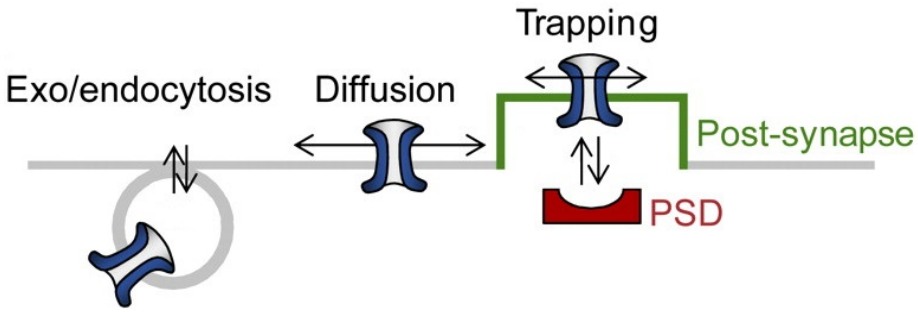

Figure 2.5: Schematic diagram of receptor trafficking mechanisms. Image: [25].

The first mechanism is *endocytosis and exocytosis* of receptors from intracellular vesicles. These are energy-consuming processes in which receptors are transported from the cell membrane into the intracellular space (endocytosis) or the other way around (exocytosis).

The second mechanism is *anchoring of receptors at the PSD* and has been the focus of numerous studies, for example [8, 26]. The PSD partially consists of scaffold proteins, which are known to bind to the receptors. This mechanism ensures trapping of receptors at the site of the PSD. Evidently, it is beneficial to ensure a higher concentration of receptors at the PSD. This gives rise to another form of compartmentalization facilitated by dendritic spines. Compartmentalization not only to isolate the spine from the rest of the dendrite for electrical signals, but also to maintain a certain concentration of surface receptors, as suggested in [1].

The third mechanism controlling receptor trafficking at synapses is *surface diffusion*. In general, receptors are not bound to the cell membrane, but can diffuse freely until being transported to the intracellular space (endocytosis) or anchored at scaffold proteins (for example at the PSD) [27].

A factor influencing how these mechanisms work is the morphology of the dendritic spine on which the synapse is located [15]. The morphology of a spine is nontrivial. The necessity of having this shape and the function of spines are not well understood. Since it is widely accepted that changes of structure of the brain are caused by changes of activity of the brain, research has focused on the implications of nontrivial morphological structures [12–15, 28].

2.2.2. EXPERIMENTAL TECHNIQUES TO INVESTIGATE RECEPTOR TRAFFICKING

Multiple experimental techniques are available to investigate the concentration and movement of surface receptors. We will discuss two widely used ones: fluorescence recovery after photobleaching (FRAP) and single particle tracking (SPT).

Fluorescence recovery after photobleaching (FRAP) is an experimental technique capable of quantifying lateral diffusion in a thin film [29]. Part of this film is photobleached by a light pulse, after which the intensity is monitored as the bleached part diffuses out and unbleached part diffuses in. Single particle tracking (SPT) is an experimental technique in which motion of individual particles in a medium is observed [30]. In the case of diffusive motion, the analysis SPT experiments can be used to provide a diffusion coefficient.

2.2.3. SYNAPTIC CROSSTALK

Crosstalk between synapses refers to instances in which components from one synapse influence the signal transmission in other synapses. An example is when a summation of neurotransmitter released in a synapse creates a spillover to other synapses and thereby creates extrasynaptic signaling [31, 32]. For specific signaling, it is important that synapses can be strengthened and weakened individually in response to their specific activity (synaptic plasticity). Synaptic crosstalk undermines the ability of the body to specifically control the strength of individual synapses.

Since receptors can diffuse across the cell membrane, they can also be a cause of synaptic crosstalk. An important question is how an exocytic event in one synapse affects the amount of receptors in neighboring synapses. In other words, if receptors are released in one spine, we would like to know what kind of implications this has on the concentration of receptors in neighboring spines. We would like to investigate the influence of the morphology of dendritic spines on this synaptic crosstalk. A model concerning this question does not exist yet. The morphology of spines is thought to cause compartmentalization enabling excitatory synapses to function as individual components and we would like to explore to what extent this occurs.

2.3. RESEARCH QUESTIONS

After this introduction to dendritic spines and their role in the nervous system, we can formulate our research question:

> How does the morphology of dendritic spines influence the synaptic crosstalk?

The subquestions belonging to this main research question are:

> How should the morphology of dendritic spines be defined?
> What constitutes a good comparison between shapes?
> What is a measure for the amount of synaptic crosstalk caused by receptor diffusion?

A model considering more than one synapse (multisynapse models) that integrates the nontrivial three-dimensional morphology that typifies dendritic spines currently does not exist. Therefore the influence of the shape of spines on their mutual interaction is not yet addressed.

3

EXISTING MODELS FOR SYNAPTIC RECEPTOR TRAFFICKING

In this chapter we explore existing models for synaptic receptor trafficking. We distinguish single synapse and multisynapse models and we make a subdivision based on how these models deal with the geometry of synapses. Furthermore, we give an overview of the methods used and discuss their results.

3.1. SINGLE SYNAPSE MODELS

As the name suggests single synapse models model the synaptic receptor trafficking considering one synapse. They typically investigate the mean first passage time (MFPT) from the top of the synapse to the dendrite and the residence time of receptors at the postsynaptic density. A variety of models exist here we discuss a selection of them.

3.1.1. HOLCMAN AND SCHUSS, 2011

Holcman and Schuss [33] took the nontrivial geometry into account and defined a domain of computation that incorporated the relatively large head and narrow neck. They use analytic methods to compute the mean first passage time from spinelike structures. More specifically, they study the residence time of a Brownian particle from the spine head to an absorbing boundary at the end of the spine neck. These particles move either on a two-dimensional (flat) or inside a three-dimensional domain. The two- and three-dimensional composite domains Ω considered consist of a head, Ω_1, connected through a small interface $\partial\Omega_i$ to a narrow cylindrical neck Ω_2 as shown in figure 3.1. The two-dimensional domain is a cross section of the three-dimensional domain. The boundary of Ω is reflecting, except the far end of domain Ω_2. Furthermore they distinguish between a bottleneck connected by a smooth funnel to the neck and a sharp connection between head and neck as in figure 3.1.

Holcman and Schuss compute the MFPT as proposed in [34] and consider a Brownian motion $\boldsymbol{x}(t)$. The expected lifetime of $\boldsymbol{x}(t)$ in Ω, given $\boldsymbol{x}(0) = \boldsymbol{x} \in \Omega$, is the MFPT $v(\boldsymbol{x})$ of $\boldsymbol{x}(t)$ from $\boldsymbol{x}$ to $\partial\Omega_a$ and the solution of the mixed boundary value problem

$$\begin{cases} \Delta v(\boldsymbol{x}) = -\dfrac{1}{D} & \text{for} \quad \boldsymbol{x} \in \Omega \\ v(\boldsymbol{x}) = 0 & \text{for} \quad \boldsymbol{x} \in \partial\Omega_a \\ \dfrac{\partial v(\boldsymbol{x})}{\partial n} = 0 & \text{for} \quad \boldsymbol{x} \in \partial\Omega_r, \end{cases} \tag{3.1}$$

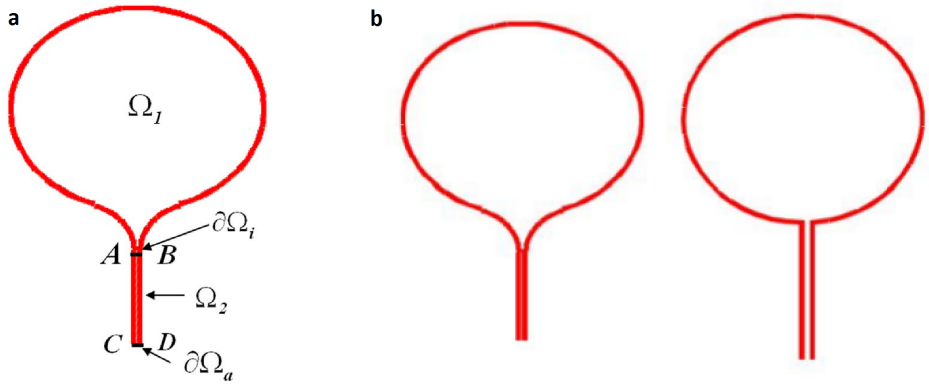

Figure 3.1: (a) The composite domain consist as used by [33]. The entire boundary is reflecting ($\partial\Omega_r$, in red), except for a small absorbing part $\partial\Omega_a$. (b) A cross section of a smooth and sharp connection.

where D denotes the diffusion constant, $\partial\Omega_r$ denotes the reflecting boundary and $\frac{\partial v(\boldsymbol{x})}{\partial n}$ is the directional derivative taken in the direction normal to the boundary at point $\boldsymbol{x}$. If the size of the absorbing part $\partial\Omega_a$ is sufficiently smaller than the reflecting part $\partial\Omega_r$, it can be shown that the MFPT is to leading order independent of $\boldsymbol{x} \in \Omega$.

Both the MFPT from the head to the interface connecting the head and the neck, $\overline{\tau}_{\boldsymbol{x}\to\partial\Omega_i}$ and the MFPT from this interface to the absorbing boundary, $\overline{\tau}_{\partial\Omega_i\to\partial\Omega_a}$ are computed. The MFPT from the head to the absorbing boundary can then be represented as

$$\overline{\tau}_{\boldsymbol{x}\to\partial\Omega_a} = \overline{\tau}_{\boldsymbol{x}\to\partial\Omega_i} + \overline{\tau}_{\partial\Omega_i\to\partial\Omega_a},$$

where the term $\overline{\tau}_{\partial\Omega_i\to\partial\Omega_a}$ equals $\overline{\tau}_{\boldsymbol{x}\to\partial\Omega_a}$ averaged over $\partial\Omega_i$, with trajectories moving into Ω_1 ending in an absorbing boundary at $\partial\Omega_i$. See [34] for further details on this computation.

The presented results include the relation between neck radius and neck length and MFPT. The geometry of the connection (smooth or sharp) affects this relationship significantly and to a larger extent in the two-dimensional than in the three-dimensional case.

DISCUSSION

The method that Holcman and Schuss present is elegant and allows an analytical representation for calculation of the MFPT. The derivation of this representation, however, is based on heavy assumptions on the geometry. For example, for diffusion on the surface of the three-dimensional domain the head is assumed to be spherical. This model considers only MFPT from the head of the spine to the exit of the spine (to the dendrite) and cannot be used for trapping at the PSD by assuming an absorbing boundary there, because of assumptions on the geometry. For more complex geometries numerical methods have to be used. Therewithal the model considers a system of one synapse and therefore cannot be used or has to be heavily adjusted to investigate the synaptic crosstalk between multiple synapses.

3.1.2. KUSTERS ET AL., 2013

Kusters et al. [1, 2] incorporated curved geometries in their work as well. They combined random walk simulations with calculations of mean first passage times to study the diffusive time scales and escape rates for different geometrical properties of the domain of computation. They consider lateral diffusion on an axisymmetric curved surface. The domain consist of a bulbous head and a funnel-like neck and is parameterized as

$$\mathcal{S}(u,\theta) = \begin{pmatrix} x(u,\theta) \\ y(u,\theta) \\ z(u,\theta) \end{pmatrix} = \begin{pmatrix} R\sin u\cos\theta \\ R\sin u\sin\theta \\ h - \frac{R\cos u}{Au} \end{pmatrix}, \quad u \in [u_{min}, \pi], \quad \theta \in [0, 2\pi],$$

where u_{min} is defined as

$$u_{min} := \arg_u \left\{ h - \frac{R\cos u}{Au} = 0 \right\}.$$

R is the maximal radial distance of the surface, h a measure for the height of the funnel, and A a shape parameter which is large for systems with a narrow neck and small for systems with a wider neck. T. For $R = 1$ and $h = 4$ the influence of A is shown in figure 3.2.

Figure 3.2: Influence of A on shape as parametrized by [1].

The in-plane Brownian motion of the particles on a curved surface is simulated using a method extensively discussed in [35]. Briefly, the random walk is produced as trajectories of fixed length steps in random directions on a curved geometry with in-plane coordinates u and θ. On a curved surface both selecting a random direction and traveling a fixed distance require some attention. A random directional unit vector $\vec{w}$ is of unit length when we subject it to the constraint $g_{uu}(w^u)^2 + g_{\theta\theta}(w^\theta)^2 = 1$, where g_{ij} are entries of the metric. Note that for axisymmetrical surfaces $g_{ij} = 0$ when $i \neq j, \quad i, j \in \{u, \theta\}$.

Next, a geodesic curve, $\boldsymbol{r}(s)$, in the direction of $\vec{w}$ is approximated, parametrized by the arc length s, using a second order approximation of the tangential plane

$$\boldsymbol{r}(s + \mathrm{d}s) \approx \boldsymbol{r}(s) + \frac{\mathrm{d}\boldsymbol{r}(s)}{\mathrm{d}s}\mathrm{d}s + \frac{1}{2}\frac{\mathrm{d}^2\boldsymbol{r}(s)}{\mathrm{d}s^2}\mathrm{d}s^2. \tag{3.2}$$

The first derivative is simply the unit tangent vector $\vec{w}$ and the second derivative is obtained by solving the geodesic equation

$$\frac{\mathrm{d}^2 r^i}{\mathrm{d}s^2} = -\Gamma^i_{kl}\frac{\mathrm{d}r^l}{\mathrm{d}s}\frac{\mathrm{d}r^k}{\mathrm{d}s}, \tag{3.3}$$

with Γ^i_{kl} the Christoffel symbols of the surface and r^i the i^{th} component of $\boldsymbol{r}$. If a step size λ is used, this method results in a shift in coordinates for every iteration given by

$$\begin{aligned}\Delta u &= w^u\lambda - \frac{1}{2}\Gamma^u_{uu}(w^u)^2\lambda^2 - \Gamma^u_{u\theta}w^u w^\theta\lambda^2 - \frac{1}{2}\Gamma^u_{\theta\theta}(w^\theta)^2\lambda^2,\\ \Delta\theta &= w^\theta\lambda - \frac{1}{2}\Gamma^\theta_{uu}(w^u)^2\lambda^2 - \Gamma^\theta_{u\theta}w^u w^\theta\lambda^2 - \frac{1}{2}\Gamma^\theta_{\theta\theta}(w^\theta)^2\lambda^2.\end{aligned} \tag{3.4}$$

This method leads to trajectories that are locally Brownian to second order in curvature. An extensive discussion of this method in general can be found in [35] and an application to this problem can be found in [2].

Kusters et al. also calculate the MFPT. They do so using almost the same mixed boundary value problem as [33]. A small modification is made however, Eq. (3.1) is substituted by

$$\nabla^2_g W = -\frac{1}{D}, \tag{3.5}$$

where D is the diffusion constant, W is the MFPT and ∇^2_g is the Laplace-Beltrami operator, which can be calculated using the metric g and Christoffel symbols. More on the metric of a surface and Christoffel symbols can be found in Section 4.1.2 and Appendix B. The more general Laplace-Beltrami operator is used to account for the curvature of the domain. With this substitution the calculation of the MFPT is equivalent for both methods.

They find a general power law dependence for both the equilibrium time scale of a population of particles and a single-particle characteristic time of escape time. The equilibrium time τ_{eq} depends on neck radius and neck length by the general relations

$$\begin{aligned}\tau_{eq} &= (\text{neck radius})^{-\alpha}, \quad \alpha > 0\\ \tau_{eq} &= (\text{neck length})^{\beta}, \quad \beta > 0.\end{aligned}$$

α and β are some positive constants and their exact value depends on the specific geometry.

DISCUSSION

The random walk method used by Kusters et al. [1, 2] is very flexible in terms of types of geometries it can be used with. As long as the metric and Christoffel symbols of the surface are available this method can be applied. In order to compute the metric and Christoffel symbols, it should be possible to calculate or (numerically) approximate first and second derivatives of the parametrization of the surface. Therefore, we require sufficiently smooth surfaces in order to apply this method.

Analytical calculation of the MFPT using Eq. (3.5) can be used to compare stochastic simulation results to. Therefore it can be used as a benchmark for the simulation results. The model presented by Kusters et al. [1, 2] focuses on one spine only. Hence, interactions between spines cannot be studied. The model is, however, suitable to be extended to a multisynapse model.

3.2. MULTISYNAPSE MODELS ON SIMPLE TWO-DIMENSIONAL GEOMETRIES

The multisynapse models that exist model dendrites as simple shapes, like flat or cylindrical surfaces. Synapses are modeled as components coinciding with the surface of the dendrite. The nontrivial shape of spines is reflected in different diffusive properties on these components, but is not explicitly taken into account. Here, we discuss some of these models.

3.2.1. CZÖNDÖR ET AL., 2012

Czöndör et al., [25], propose a model that uses random walk simulation on a flat surface. The model takes the three major mechanisms of receptor trafficking into account: surface diffusion, anchoring at the postsynaptic density, and endo/exocytic recycling of receptors. They define a flat working space, we call Ω, of length L and width w with rebound conditions on each side. Postsynaptic spines are modeled as square obstacles with lower diffusion constant and each synapse contains a square PSD which allows trapping. Also exocytic and endocytic events were introduced.

Surface diffusion was modeled by updating the positions $x(t)$ and $y(t)$ of a particle each time step by incrementing them by $\sqrt{2D\Delta t}Z_x$ and $\sqrt{2D\Delta t}Z_y$ respectively, were Z_x and Z_y are realizations of a standard normal distribution. This comes down to a simple application of the Euler-Maruyama method to the stochastic differential equation

$$\mathrm{d}\boldsymbol{X}_t = \sqrt{2D}\,\mathrm{d}\boldsymbol{W}_t,$$

where $\boldsymbol{W}_t$ is a Wiener process. This represents two-dimensional diffusion of a single particle with constant diffusion coefficient D and without convection. The mean squared displacement for each time step and each particle is therefore $\mathbb{E}\left[||\boldsymbol{X}_{t+\Delta t} - \boldsymbol{X}_t||^2\right] = 4D\Delta t$. The corresponding diffusion equation is the two-dimensional diffusion equation with constant diffusion coefficient D and no convection

$$\frac{\partial c(\boldsymbol{r},t)}{\partial t} - D\Delta c(\boldsymbol{r},t) = 0, \quad \boldsymbol{r} \in \Omega.$$

If a receptor reached a postsynaptic area, it was set to diffuse with a lower diffusion coefficient. The simulation method remains otherwise the same. Whenever a receptor reached a PSD area, binding to the PSD was modeled by a random variable with a Bernoulli distribution with success probability proportional to the time step Δt and a certain predefined rate k_{on}. During binding the receptor was set to diffuse with an even lower diffusion coefficient. Detachment was modeled using a random variable with Bernoulli distribution with success probability proportional to the time step, but with a possible different rate, k_{off}, than for binding.

To mimic exocytic events, new trajectories were initiated. Here, the number of receptors, exocytic site, timing and frequency of an exocytosis were specified.

To simulate endocytic events square endocytic zones (EZs) were introduced. The event of absorption is thereafter modeled in the same way as anchoring at the PSD, by a random variable with a Bernoulli distribution with success probability proportional to the time step and a certain predefined rate k_{endo}.

Czöndör et al. present results of their simulation in which they consider the influence of (extra)synaptic endo/exocytic events on the receptor concentration in surrounding synapse(s). Furthermore, the outputs of the simulation are directly comparable to single particle tracking (SPT) and fluorescence recovery after photobleaching (FRAP) experiments and can therefore be easily benchmarked.

DISCUSSION

The work of Czöndör et al. in [25] incorporates the three major mechanisms influencing synaptic receptor trafficking. It is very useful that their results are directly comparable to SPT and FRAP data.

They model synapses as flat surfaces which is not the typical shape of spines belonging to excitatory synapses. However, the way trapping is modeled here can be integrated in a model that incorporates the typical three-dimensional shape. The model allows for integration of multiple synapses, however, they do not regard synaptic crosstalk.

In an equilibrium situation, Czöndör finds higher concentrations in the postsynaptic area. The explanation is sought in the lower diffusion coefficient at this area. We want to review this. Take a two-dimensional diffusion problem with a location dependent diffusion coefficient $D(\boldsymbol{r})$,

$$\frac{\partial c(\boldsymbol{r},t)}{\partial t} = \nabla\left[D(\boldsymbol{r})\nabla c(\boldsymbol{r},t)\right], \quad \text{for } (\boldsymbol{r},t) \in (\Omega, \mathbb{R}^+),$$

with boundary conditions,

$$frac\partial c(\boldsymbol{r},t)\partial n = 0 \quad \text{for } \boldsymbol{r} \in \partial\Omega$$

and initial condition,

$$c(\boldsymbol{r},0) = c_0(\boldsymbol{r}) \quad \text{for } \boldsymbol{r} \in \Omega.$$

We see that $c(\boldsymbol{r},t) := \frac{\int_\Omega c_0(\boldsymbol{r})\,\mathrm{d}\Omega}{\int_\Omega \mathrm{d}\Omega}$ is an equilibrium solution for this system. Because of uniqueness, it must be the unique solution to this system. Czöndör, however, finds a non-constant (and noncontinuous) equilibrium solution. This is because the continuum mechanics counterpart of the stochastic process that is simulated, is not the diffusion equation, but the Fokker-Planck equation,

$$\frac{\partial c(\boldsymbol{r},t)}{\partial t} = \nabla^2\left[D(\boldsymbol{r})c(\boldsymbol{r},t)\right].$$

A extensive analysis of stochastic differential equations and diffusion processes can be found in [36]. This is an illustration of how easily a different diffusion process is implemented when using an ad hoc manner to simulate stochastic differential equations.

3.2.2. BRESSLOFF ET AL., 2008

Bressloff et al. [37] proposed a model in which they model a dendrite as a two-dimensional cylindrical surface with small, partially absorbing holes, which represent the transverse intersections of the spines with the dendrite. In [37], they present an extension of their work in [38] where a model of receptor trafficking at a single dendritic spine is treated.

They formulate a diffusion-trapping model on a cylinder with length L and radius l. They neglect the extrinsic curvature of the membrane because protein receptors and spine necks are much smaller than the circumference of the cylinder. Therefore, they represent their surface as a long rectangular domain Ω_0,

$$\Omega_0 = \{(x,y) : 0 < x < L, |y| < \pi l\}.$$

Here, x is the coordinate in the direction of the axis of the cylinder and y is the coordinate in the radial direction of the cylinder. At $x = 0$ they impose a nonzero flux boundary condition, which represent a constant inflow of of new receptors. On the other end, at $x = L$, they impose a no-flux boundary condition, modeling a reflecting boundary. On $y = \pm\pi l$ they impose periodic boundary conditions,

$$c(t,(x,y+2k\pi l)) = c(t,(x,y)), \quad k \in \mathbb{Z}.$$

Each spine neck is modeled as a circular intersection with radius ϵ, Ω_j, where j labels the j^{th} spine. The surface of the cylinder excluding these small discs is denoted by $\Omega_\epsilon = \Omega_0 \setminus \cup_{j=1}^N \Omega_j$. Because of the small area of each spine, they assume the receptor concentration within each spine to be spatially homogeneous and equal to $\tilde{c}_j$ for spine j. The dendritic surface receptor concentration evolves according to the diffusion equation

$$\frac{\partial c}{\partial t} = D\nabla^2 c.$$

On the boundary of each Ω_j, $\partial\Omega_j$, they impose the mixed boundary condition

$$\epsilon\partial_n c(\boldsymbol{r},t) = -\frac{\omega_j}{2\pi D}\left(c(\boldsymbol{r},t) - \tilde{c}_j\right), \quad \boldsymbol{r} \in \partial\Omega_j, \quad j = 1,\ldots,N,$$

where $\partial_n c$ is the outward normal derivative to Ω_ϵ. The physical interpretation is that the flux of receptors between a specific spine and the dendrite depends on the difference in concentration between either side of the boundary with ω_j as effective hopping rate. A pair of differential equations determines the value of $\tilde{c}_j$ over time. These equations are not discussed here, but an extensive review of the full method can be read in [37]. The initial condition that concludes this model is

$$c(\boldsymbol{r},0) = \delta(\boldsymbol{r} - \boldsymbol{r}_0), \quad \text{for some } \boldsymbol{r}_0 \in \Omega_\varepsilon.$$

An analysis of this model is done by constructing the steady-state solution using singular perturbation techniques. These results are compared with numerical solutions of the full model and with a reduced one-dimensional model.

They show that for long, thin dendrites the variation of the receptor concentration around the circumference of the dendrite is negligible so that the dendrite can be modeled a simpler one-dimensional cable. They remark that the difference between the one and two-dimensional can become significant in the case of short dendrites with few spines. Further, they note that an important extension of their work would be to consider a much more detailed model of receptor trafficking within each spine.

DISCUSSION

The paper of Bressloff et al., [37], is the most mathematical work considered. They give an extensive analysis of their model and verify their results.

This work does not investigate how (the shape of) spines influence their own concentration or the concentration in neighboring spines. Moreover, they assume a constant inflow of receptors at one side of the domain and do not explore the effect of the precise location of exocytosis.

3.2.3. OTHER MULTISYNAPSE MODELS

More multisynapse models do exist, but we will not give an extensive review of these.

Holman and Triller (2006), [39], propose a two-dimensional model in which they account for binding to scaffolding molecules in the PSD and the presence of obstacles to diffusion. They derive Markovian equation and analyze steady-state solutions. They argue that when the fluxes involve a sufficiently large number of receptors, the dynamics of the receptors can be modeled using standard differential equations of chemical reactions and a system of differential equations is proposed and analyzed. Furthermore they suggest a way to use the model to interpret FRAP data.

Earnshaw and Bressloff propose a model in [40] that is similar to their work in [37], discussed in section 3.2.2, but also integrates binding of receptors to scaffold molecules in the PSD.

3.3. MULTISYNAPSE MODELS INTEGRATING THREE-DIMENSIONAL MORPHOLOGIES

Multisynapse models integrating three-dimensional morphologies do not exist yet. Furthermore, a model assessing the synaptic crosstalk between dendritic spines is lacking. In order to answer our research questions, we created such models. In Chapter 4 we present them.

4

TWO MULTISYNAPSE MODELS INTEGRATING THREE-DIMENSIONAL MORPHOLOGIES

In order to answer the research questions posed in Section 2.3, we use two different models of diffusion. The first one is an atomistic, particle-based approach in which diffusion is seen as distinct particles undergoing Brownian motion, the second one is a continuum mechanics approach in which we start from Fick's laws and their mathematical implications. Of course, these two are heavily related: in a environment where a enormous number of individual particles undergo diffusion, randomness gets undetectable if we measure the concentration of these particles. Simulating an enormous amount of particles and keeping track of the concentration of these particles should therefore produce the same result.

These two notions of diffusion underlie the two models we developed. The first model regards diffusion as a collection of individual particles undergoing Brownian motion. In other words, the behavior of single particles is prescribed as a stochastic process and the state of the total system is the collection of the state of all individual particles. We will call this model the *stochastic particle-based model*. The second model is based on an application of Fick's laws, a system of partial differential equation. These laws model (pure) diffusion as the movement of a substance from regions of higher concentration to regions of lower concentration. This model does not simulate individual particles, but merely the concentration of particles. We will call this model the *concentration-based model*, also known as a continuum-scale model.

The reason we use two models to model essentially the same thing is two fold. First of all, the stochastic particle-based model gives us insight into the statistics that are inextricably linked to a diffusion process. First and second moments of first passage times are important statistics we would like to calculate and these (stochastic) quantities are determined more easily in the framework of a model with stochastic nature. On the other hand, simulating a stochastic process on a curved surface is hard [35, 41]. Methods based on projecting a stochastic process on a flat surface onto a curved surface have to be handled with care, because approximation errors pile up quickly, whereby such techniques almost certainly represent a different diffusion process than was intended [35]. We have seen an example of such a miss match between intended and simulated process in Section 3.2.1. Because of this, we would like to benchmark it against one that does not use stochastic processes, but a numerical solution to partial differential equations instead. Furthermore, when interested in concentrations, a particle-based model needs a lot of particles to simulate concentrations with a reasonably low influence of randomness. Therefore a concentration-based model will be less computational intensive in such cases.

Before getting into the details of these methods, we discuss the components of the models which are the same for both. This is primarily the geometry of the domain we regard and the way we would like to deal with the notions of receptor trapping and endo-/exocytosis.

4.1. GEOMETRY OF THE DOMAIN

In general, we consider a domain that consists of a dendrite and n dendritic spines distributed along the dendrite. The dendrite is modeled as a cylinder of length l and radius R_d. Since protein receptors are much smaller than the circumference of the cylinder, we neglect the extrinsic curvature of the membrane. Therefore, as shown in Figure 4.1, the surface of the dendrite is represented as a rectangular domain Ω_0,

$$\Omega_0 := \{(x,y) \mid 0 < x < l\,, \quad |y| < \pi \cdot R_d\}\,.$$

The boundary of this domain is denoted with Γ. The cylindrical property is preserved by imposing periodic boundary conditions on $y = \pm\pi \cdot R_d$. On this cylindrical surface dendritic spines are located. Each spine intersects the surface, such that the intersection is a closed disc Ω_j^{base} of radius R_j^{exit} around the coordinate $\boldsymbol{r}_j = (x_j, y_j)$. Its boundary is called $\partial\Omega_j$,

$$\begin{aligned} \Omega_j^{base} &:= \left\{ \boldsymbol{r} = (x,y) \in \Omega_{dendrite} \;\middle|\; |\boldsymbol{r} - \boldsymbol{r}_j| \le R_j^{exit} \right\}, \\ \partial\Omega_j &:= \left\{ \boldsymbol{r} = (x,y) \in \Omega_{dendrite} \;\middle|\; |\boldsymbol{r} - \boldsymbol{r}_j| = R_j^{exit} \right\}. \end{aligned}$$

Furthermore, the surface of the cylinder Ω_0, excluding the discs Ω_j is denoted by $\Omega_{dendrite}$, so that

$$\Omega_{dendrite} = \Omega_0 \setminus \bigcup_{j=1}^{n} \Omega_j^{base}.$$

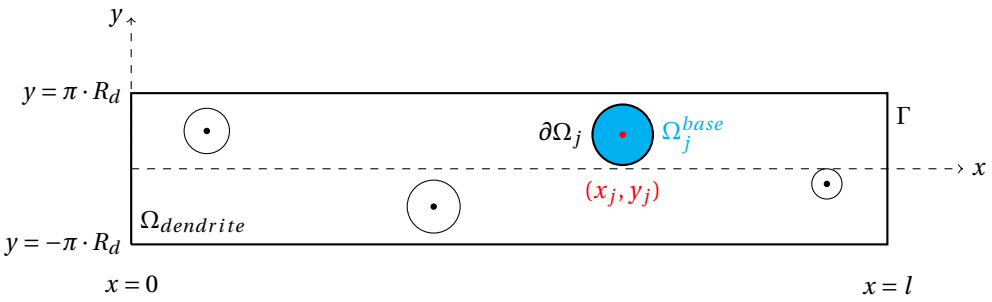

Figure 4.1: Top view of domain of computation.

The domain of computation is an union of the domain $\Omega_{dendrite}$ and the dendritic spines Ω_j. The dendritic spines are modeled as out-of-plane protrusions of this surface. The morphology of these spines will be discussed in the next section.

4.1.1. MORPHOLOGY OF DENDRITIC SPINES

The dendritic spines are modeled as out-of-plane protrusions of the surface $\Omega_{dendrite}$. They intersect the dendritic surface, such that the domain of intersection is Ω_j^{base}. Since it is not yet completely understood how dendritic spines develop into their specific shape, there is no one clear answer to the question how we should define their geometry. In order the investigate the effect of the characteristic shape of dendritic spines on the diffusion process of receptors, we would like to have a definition that incorporates these characteristics. The unpublished work of Miermans, Kusters & Storm [42] does that.

They use a Canham-Helfrich model to model the shape of membrane protrusions. This model is based on a minimum energy principle. At equilibrium, the free energy of the shape is minimized. Canham [43] proposed

that the behavior of membranes is governed by minimizing the bending energy. Helfrich [44] built on this model and gave a more precise formulation.

Here, we give a brief explanation of the method of Miermans [42]. At $t = 0$ they define a flat membrane and fix a circle with radius 1 on it, in Figure 4.2 denoted by Γ. The surface area $\mathcal{A}$ of the membrane enclosed by this circle is in this state $\mathcal{A}_0 = \pi$. Then an iterative method is used to determine the shape of the membrane in subsequent time steps. Every time step the surface area $\mathcal{A}$ is incremented while its boundary, Γ stays fixed in plane. By minimizing the free bending energy the shape of the membrane is computed. This results in an out-of-plane deformation of the part of the domain that is within these boundaries (the blue domain in Figure 4.2). Boundary conditions are imposed on Γ to ensure smoothness of the membrane and to keep the boundary Γ at its fixed location. The solution on each time step is obtained solving a constrained minimization problem using Lagrange multipliers.

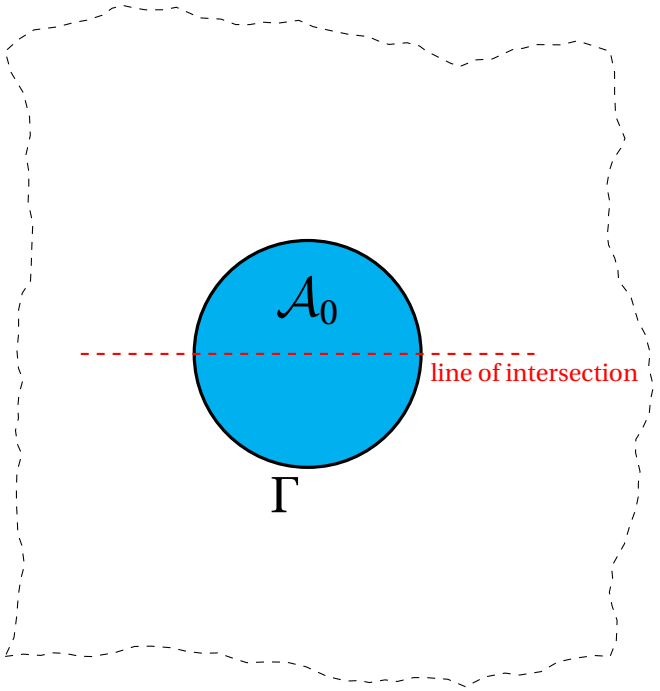

Figure 4.2: Top view of working space of Miermans et al. The blue disk, enclosed by Γ, is incrementally swollen every iteration, which results in an out-of-plane deformation (not shown here). The red line indicates the place where the intersections shown later are located.

The result of the described method are protrusions of the membrane as shown in Figure 4.3. It can be seen that as the surface swells, characteristic features like a thin neck and large head form. The downside is that we do not see long necks with this method, incorporating long necks can be an extension in future research.

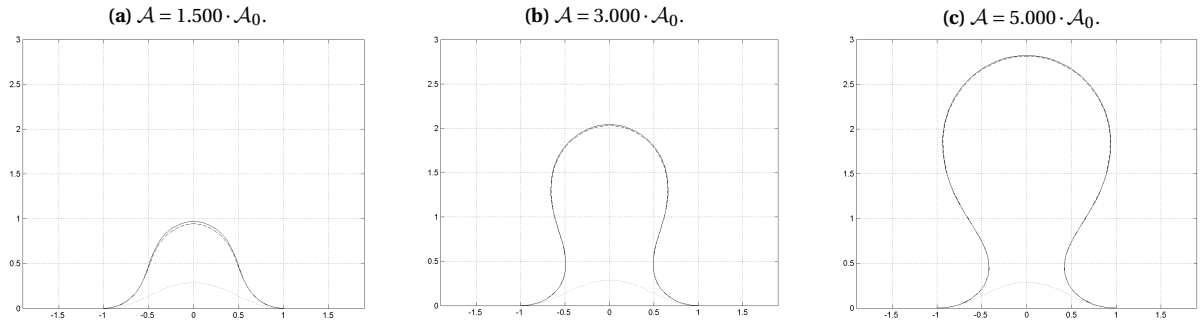

Figure 4.3: Intersection of shapes for selected values of the surface area $\mathcal{A}$ as a multiple of the original surface area $\mathcal{A}_0$. Intersection is taken at the location of red dashed line in Figure 4.2. Results produced by [42].

The total domain of computation is the union of the cylindrical dendrite $\Omega_{dendrite}$, the dendritic spines Ω_j and the borders between spines and dendrite $\partial\Omega_j$ and is denoted by Ω,

$$\Omega = \Omega_{dendrite} \cup \bigcup_{j=1}^{n} \{\Omega_j \cup \partial\Omega_j\}.$$

Surface receptors undergo a diffusion process defined on this domain Ω.

4.1.2. FORMALIZATION OF THE DOMAIN

We use a global parametrization $\mathcal{S}(\alpha,\beta)$ for the surface,

$$\mathcal{S}(\alpha,\beta) := \begin{pmatrix} x(\alpha,\beta) \\ y(\alpha,\beta) \\ z(\alpha,\beta \end{pmatrix},$$

with the associated metric

$$g_{\alpha\beta} := \begin{pmatrix} \mathcal{S}_\alpha \cdot \mathcal{S}_\alpha & \mathcal{S}_\alpha \cdot \mathcal{S}_\beta \\ \mathcal{S}_\beta \cdot \mathcal{S}_\alpha & \mathcal{S}_\beta \cdot \mathcal{S}_\beta \end{pmatrix}, \tag{4.1}$$

where $\mathcal{S}_i$ are partial derivatives of $\mathcal{S}(\alpha,\beta)$. From this we can calculate the Christoffel symbols Γ^k_{ij} as

$$\Gamma^k_{ij} = \sum_{m=\alpha,\beta} \frac{1}{2} g^{km} \left(\frac{\partial g_{mi}}{\partial j} + \frac{\partial g_{mj}}{\partial i} - \frac{\partial g_{ij}}{\partial m} \right), \qquad i,j,k = \alpha,\beta,$$

where g_{ij} are entries of the of the metric $g_{\alpha\beta}$ and g^{ij} entries of the matrix inverse to the metric $g_{\alpha\beta}$ from Eq. (4.1).

A complete derivation of the parametrization of the surface can be found in Appendix B.

4.1.3. BOUNDARIES

The domain as defined in the previous section and shown in Figure 4.1 has multiple boundaries with associated boundary conditions. There are three boundaries we distinguish:

- The boundaries at $x = 0$ and $x = l$;
- The boundaries at $y = \pm\pi \cdot R_d$;
- The optional boundary at the site of a PSD.

The first type, the boundaries at $x = 0$ and $x = l$ are the ends of the cylinder, but do not model the ends of the dendrite. The dendrite runs to the cell body on one side and continues on the other side until it reaches its end. Therefore, in practice, receptors can leave and enter our domain through these boundaries. Nevertheless, we choose full reflection at these boundaries. The reason we do this is twofold. The processes we study inside our domain of computation are similar to the processes that take place on the dendrite just outside these boundaries (so at $x < 0$ and $x > l$), therefore we can assume that as many receptors enter and leave through either of these boundaries and for simplicity we can model this behavior as reflection. The second ratification is that, as will be explained in Chapter 5, we have a preference for a closed system, in which mass is conserved. Reflective boundary conditions ensure that. Periodic boundary conditions would also ensure

mass conservation, but are unsuitable, because they couple left and right boundary, for which there is no physical basis.

As mentioned we choose periodic boundary conditions for the boundaries at $y = \pm\pi \cdot R_d$. Since our domain represents a cylinder, this is a natural choice.

In some test cases a boundary is defined at the site of the boundary of the PSD. In other words, the PSD will not be part of the domain of computation in these cases. If so, these boundaries are completely absorbing boundaries. The optional boundaries at the site of a PSD need a bit more explanation. We will elaborate on this, when discussing the designed models.

4.1.4. MECHANISMS OF RECEPTOR TRAFFICKING

In Section 2.2.1 we have discussed the three major mechanisms with which receptor traffic is regulated. Both our models integrate three major components of receptor trafficking: surface diffusion, anchoring at the postsynaptic density and exocytosis.

ANCHORING AT THE PSD

The mechanism a nerve cell employs to anchor receptors to the postsynaptic density is modeled in two ways. Firstly, by including the binding and unbinding process taking place at the PSD, schematically shown in Fig 4.4a. In this case the receptors are allowed to undergo reversible binding at the site of the PSD. Although the PSD contains different domains with possibly different binding characteristics, these interactions were simplified and comprehended in a binding rate, k_{on}, and a dissociation rate, k_{off}, thus adopting the same approach as Czöndör et al. [25]. The values of these binding rates were chosen according to the study of [25] and have unit $[s^{-1}]$. In modeling the PSD we do not account for a possible saturation of scaffold molecules in the PSD. This means that the rates k_{on} and k_{off} are time and concentration independent.

The second manner in which we account for the presence of the PSD is to model its boundary as an absorbing boundary. A schematic diagram of this version of the model is given in Fig. 4.4b. The motivation behind this approach is that the time a receptor (typically AMPA and NMDA receptors) spends at the surface of the cell membrane before undergoing endocytosis is limited [45]. The receptors can diffuse freely for a limited time until being transported to the intracellular space, where they are disintegrated or transported for exocytosis elsewhere. Since this lifetime is limited and the number of synapses in which a receptor can reside is constrained, the first PSD it encounters after exocytosis is the most relevant one.

(a) Trapping at the PSD. The parameters concerning trapping are k_{on} and k_{off}.

(b) Absorption at the boundary of the PSD.

Figure 4.4: Schematic diagram of the model including surface diffusion and trapping (left) or absorption (right) at the boundary of the PSD. Original in [25].

EXOCYTIC AND ENDOCYTIC EVENTS

Exocytic events occur at the beginning of a simulation in our models. They are regarded as initial conditions. For the stochastic particle-based model this means trajectories of individual particles are initiated at the location of exocytosis. For the concentration-based model this means that at the beginning of the simulation the concentration is elevated on the location of exocytosis. Two locations for exocytosis are distinguished: spinal exocytosis and dendritic exocytosis. This resembles actual processes in neurons. The release of recep-

tors from the intracellular space to the cell membrane are both observed on the dendritic surface, as well as in spine heads [46].

We do not introduce exocytic events during a simulation, although it would be possible in both models. In the particle-based model trajectories would have to be initiated during the course of a simulation, in the concentration-based model, exocytic events could be seen as a time-dependent source term. Since we are not investigating the influence of different frequencies or locations of exocytosis in one simulation, this feature is left out. If needed in the future, this would be relatively easily to implement.

We do not designate locations for endocytosis. We are interested in the effect of the shape of dendritic surface on the diffusion process of receptors after exocytosis, before the receptor is transported back into the intracellular space.

4.1.5. PARAMETERS

Both models use a number of parameters. Model parameters and their origin are given in Table 4.1. The diffusion coefficient D is a function of the temperature, the viscosity of the medium and the geometrical properties of the diffusing particles. Here, we choose the value of D corresponding to estimated values from experiments in [25].

Category	Parameter	Notation	Value	Dimension	Source
Dimensions of geometry	Dendrite width	w	2.5	μm	This study.
	Dendrite length	L	5	μm	This study.
	Exit radius spine	R_{exit}	1	μm	[47]
	Spine spacing	a	2.5	μm	[48]
	Radius of PSD	R_{PSD}	0.2	μm	[47]
Positions	Exocytic location	(x_0, y_0, z_0)	varying, see text.	μm	[46]
Numbers	Number of receptors	N_{part}	$10^4 - 10^6$	-	This study.
Times	Time step	Δt	$2.5 \cdot 10^{-4}$	s	This study.
	Duration of simulations	T_{end}	varying, see text.	s	This study.
Diffusion coefficients	Diffusion coefficient	D	0.1	$\mu m^2/s$	[49] *
Kinetic rates	Receptor binding rate	k_{on}	20	s^{-1}	[25]
	Receptor dissociation rate	k_{off}	1	s^{-1}	[25]

Table 4.1: Model parameters for simulations.

4.2. MODEL I: STOCHASTIC PARTICLE-BASED MODEL

In this section we present the stochastic particle-based model that we designed and implemented. We represent particles as non-interacting point particles. They do not interact with each other, meaning they can pass each other freely and even – theoretically – be at the same position at the same time. Of course, this is physically incorrect. Receptors have nonneglectable dimensions and interact with other receptors as well as other proteins present in the cell membrane. However, since we are interested merely in the effect of the curvature of the surface on the diffusion process of neurotransmitter receptors, we neglect these interactions.

The particles are subjected to random movement that can be described using a stochastic differential equation, Brownian motion. The aim of this method is simulating the in-plane Brownian motion of particles on a curved surface. This results in a random walk simulation of which the details will be made clear in this section.

4.2.1. STOCHASTIC PROCESSES ON CURVED SURFACES

Our domain of computation, Ω can be seen as a two-dimensional Riemannian manifold $\mathcal{B}$ equipped with a Riemannian metric g. This metric defines a volume measure on $\mathcal{B}$, which we denote with dVol_g. If a diffusion

process defined on the manifold $\mathcal{B}$ is defined by an elliptic operator and the process conserves the integral of the diffusion quantity with respect to dVol_g, then the adjoint operator of L, L^* is the generator of a stochastic process corresponding to the diffusion process intended. A review of the basics underlying the construction of diffusion on manifolds can be found in [41].

4.2.2. SIMULATING STOCHASTIC PROCESSES ON CURVED SURFACES

Simulating a diffusion process on a curved surface is not trivial. Diffusion processes on manifolds are often established by projecting a stochastic process on a flat space onto the surface. Solutions can than be obtained by considering the flow of diffeomorphisms on the surface [36]. But for irregular surfaces such analytic techniques are too complex to constitute a realistic solution. Christensen [35] states that in such cases extreme care has to be taken, because otherwise a different diffusion operator is represented from what was initially intended.

Christensen proposes an approach to simulations of diffusive processes in general, which can also be applied to diffusion on general manfolds. He introduces a Monte Carlo type method with simulates the paths of single particles. We give a brief summary of the principles on which this method is based and an insight in our implementation. We focus on an application of this method to diffusion with an constant (and isotropic) diffusion tensor.

The method of [35] is based on the observation that every Monte Carlo update scheme moving a particle from $\boldsymbol{r}_0$ to $\boldsymbol{r}$ in a time interval Δt prescribes a certain transition rate and that a correct numerical method matches the first and second moments of this transition rate to the ones of the original diffusion equation.

The method of Christensen starts of with an equation describing the development of a particles probability distribution P over a surface $\mathcal{B} \in \mathbb{R}^3$, with constant and scalar diffusion tensor D

$$\frac{\partial P}{\partial t} = D\nabla_g^2 P.$$

Here, ∇_g^2 is the Laplace-Beltrami operator associated with the metric g. The Laplace-Beltrami operator can be expressed in the coordinates associated with the manifold $\mathcal{B}$

$$\nabla_g^2 P = \frac{1}{\sqrt{|\det g|}} \sum_{i,j=1}^{2} \partial_i \left(\sqrt{|\det g|} g^{ij} \partial_j P \right), \quad i,j = 1,2, \tag{4.2}$$

where g_{ij} are entries of the of the metric g and g^{ij} entries of the matrix inverse to the metric g.

An update routine is constructed, involving two spatial and two temporal components specified in Table 4.2. $f(\xi)$ and l together represent the radial jump distribution in the physical space and $h(\zeta)$ and τ represent the distribution of waiting times between successive jumps.

Component	**Description**
ξ	dimensionless radial jump length
$f(\xi)$	dimensionless radial distribution
$l > 0$	typical jump length
ζ	dimensionless temporal jump length
$h(\zeta) > 0$	dimensionless temporal distribution
$\tau > 0$	time scale

Table 4.2: Components representing jump distribution in physical space and waiting times between jumps of method proposed by Christensen [35].

The moments of $f(\xi)$ and $h(\zeta)$ are denoted by $\overline{\xi^m}$ and $\overline{\zeta^m}$ respectively. Furthermore, the dimensionless (scalar) diffusion tensor $b = D\overline{\zeta}\tau / \overline{\xi^2} l^2$ is introduced. Now, we provide the update mechanism that imple-

ments the simulation of a moving particle from a starting position $(\boldsymbol{r}, t)$ to $(\boldsymbol{r}+\Delta\boldsymbol{r}, t+\Delta t)$ in an n-dimensional environment. The procedure is given in Alg. 1.

Algorithm 1 Algorithm as presented by [35].

Initialization: Calculate $b = D\overline{\zeta}\tau / \overline{\xi^2} l^2$.

1: Draw a dimensionless waiting time ζ from distribution h and set $\Delta t = \zeta\tau/(2n)$.
2: Choose a test step $\Delta\boldsymbol{r}$:
   a. Choose a unit vector $\boldsymbol{w}$ from a uniform distribution over all directions.
   b. Choose a dimensionless, radial jump length ξ from distribution f.
   c. Calculate $\Delta\boldsymbol{r}$ by moving a length $|\sqrt{b}\boldsymbol{w}|\xi l$ along a geodesic in the direction of $\boldsymbol{w}$.
3: Update $(\boldsymbol{r}, t) \longrightarrow (\boldsymbol{r}+\Delta\boldsymbol{r}, t+\Delta t)$.

Analytic solutions of a geodesic are not generally found. However, if the jump length is small enough, good approximations can be easily obtained using a Taylor expansion.

4.2.3. SIMPLIFICATIONS AND IMPLEMENTATION

Simplifications to the scheme of [35] are possible. Christensen recommends to use fixed steps in space and time, because any couple of distributions f and h will do if l is small enough. We adopt this recommendation and fix a spacial step size λ. Furthermore, since we consider diffusion on a surface we fix the dimension $n = 2$. Alg. 1 then reduces to Alg. 2.

Algorithm 2 Algorithm as presented by [35], adapted to a fixed spacial step size λ.

Initialization:
   Fix a spacial step size $\lambda > 0$.
   Set $\Delta t = \lambda^2/4D$.

1: Choose a test step $\Delta\boldsymbol{r}$:
   a. Choose a unit vector $\boldsymbol{w}$ from a uniform distribution over all directions.
   b. Calculate $\Delta\boldsymbol{r}$ by moving a length λ along a geodesic in the direction of $\boldsymbol{w}$.
2: Update $(\boldsymbol{r}, t) \longrightarrow (\boldsymbol{r}+\Delta\boldsymbol{r}, t+\Delta t)$.

A geodesic curve parametrized by arch length s can be approximated in the same way [2] did, as given in Eq. (3.2). The Taylor expansion used is

$$\boldsymbol{r}(s+\mathrm{d}s) = \boldsymbol{r}(s) + \frac{\mathrm{d}\boldsymbol{r}(s)}{\mathrm{d}s}\,\mathrm{d}s + \frac{1}{2}\frac{\mathrm{d}^2\boldsymbol{r}(s)}{\mathrm{d}s^2}\,\mathrm{d}s^2 + \mathcal{O}(\mathrm{d}s^3). \tag{4.3}$$

If the spatial step size λ is small enough, leaving out the $\mathcal{O}(\mathrm{d}s^3)$-term in Eq. (4.3) constitutes a good approximation. The second order terms can be calculated as in Eq. (3.3). The resulting updating scheme for the positions is then given by Equation (3.4).

4.2.4. MODELING ANCHORING AT THE PSD

Binding and unbinding at the PSD are comprehended in the two rates k_{on} and k_{off}. These rates are measures for how big the probability is that in a certain time interval Δt the probability of binding and unbinding is. Additionally, this probability should be proportional to the size of this time interval. These notions are incorporated in the following implementation.

Whenever a receptor reaches a PSD area, binding to the PSD is modeled by a random variable with a Bernoulli distribution with success probability equal to the product of the time step Δt and the binding rate k_{on}. While a receptor is bound to the PSD, it remains static and does not move. Detachment is modeled using a random variable with Bernoulli distribution with success probability equal to the product of the time step and the dissociation rate, k_{off}.

4.2.5. INTRODUCING AN EXOCYTIC EVENT

An exocytic event occurs at the beginning of a simulation only, it serves as an initial condition. For the stochastic particle-based model this means that trajectories of receptors are initiated at the location of exocytosis. We can decide per individual receptor where its trajectory starts, we are not bound to grid points or finite dimensional spaces in which a solution has to be sought. This makes this method a very flexible one.

In our simulation we release all receptors at once, at time zero. If required, our model allows for multiple exocytic events during the lifetime of a simulation as well as a continues release of receptors over some time interval. The location of exocytosis can differ per event and per receptor. There is a lot of flexibility, which makes this method such a powerful tool. The location of such events in our simulation will differ per experiment, since we would like to consider both the effect of spinal as well as dendritic exocytosis. Naturally, when presenting results, the details of the setup are given.

4.2.6. BOUNDARY CONDITIONS

An additional advantage of this implementation is that boundary conditions like reflection, absorption or a mixture of the two are easily implemented. Since the paths of single particles are simulated we can apply the boundary conditions per individual particle. If a particle encounters a reflecting boundary, geometrical rules of reflection can be applied. If a particle encounters an absorbing boundary, it is removed from the system.

Special care has to be taken when a particle reaches a transition between domains, typically when it reaches the boundary of a spine while diffusing over the dendrite or vice versa. Diffusion on the different domains Ω_0 (dendrite) and Ω_j (spines) are handled separately, since the metric corresponding to the spine surface is more complicated than the metric of the dendritic surface, which is a flat surface. However, for particles reaching the intersection between the two ($\partial\Omega_j$) a methodology for transition has to be developed. Details can be found in Appendix D.

4.3. MODEL II: CONCENTRATION-BASED MODEL

In this section we present our other, concentration-based model. As will come apparent later, this model will help us answer some of the research questions easier than the first model. Whereas the particle-based model is ideal for measuring first passage times and its statistics, this model needs to simulate a big number of particles if we would like to have information on concentrations at different locations and times. The reason is that due to stochastic variations concentration levels will fluctuate and randomness only gets negligible when a lot of particles is used or – in the case of an equilibrium – the mean is taken over a large number of time steps after reaching equilibrium. With a large number of particles this model gets computationally cumbersome and an alternative is appreciated. Furthermore, we would like to benchmark our first model to this one, thus validating it.

This model is based on a system of partial differential equations that model the diffusion process. The unknown quantity is the concentration of surface receptors within the domain of computation. Because we are dealing with a non-trivial geometry, our system cannot be solved analytically and we will need numerical methods to solve it. We choose for the application of a finite element method (FEM) and discuss how simulations are set up. Additionally the way the notions of trapping and exocytosis are dealt with will be explained.

The weak formulation and discretization used for the FEM scheme can be found in Appendix 6. The implementation and execution of the FEM-scheme is handled by Nutils, an open source Python programming library for finite element applications. More information on Nutils can be found on nutils.org. The software package can be downloaded on GitHub: github.com/nutils.

4.3.1. GOVERNING EQUATIONS

On the domain of computation Ω surface receptors are allowed to diffuse freely. Let $C(\boldsymbol{r},t)$ denote the concentration of surface receptors within the domain of computation. The receptor surface concentration evolves according to the diffusion equation

$$\frac{\partial C}{\partial t} = D\nabla^2 C, \quad (\boldsymbol{r},t) \in \Omega \times \mathbb{R}^+,$$

where D is the diffusion coefficient and ∇^2 denotes the Laplace-Beltrami operator. This operator is consistent with the Laplace-Beltrami operator of Eq. (4.2). It is a generalized version of the Laplace operator and operates on functions defined on surfaces in Euclidean space or – more generally – on Riemannian manifolds.

4.3.2. MODELING ANCHORING AT THE PSD

Within this model we deal with the notion of trapping by modeling a binding process at the postsynaptic density. In order to incorporate binding, we define two new quantities: the concentration of *free* surface receptors, $C_F(\boldsymbol{r},t)$, and the concentration of *bound* surface receptors, $C_B(\boldsymbol{r},t)$.

At the site of a PSD, free surface receptors can change into bound surface receptors, thereby losing their diffusive properties. The rate with which this happens is proportional to the concentration of free surface receptors and the binding rate, k_{on}. This process serves as a positive source term for function of the concentration of bound particles and as negative source term (well) for the concentration of free particles. The other way around, at the site of a PSD, bound receptors can change into free surface receptors, regaining diffusive properties. This process is proportional to the concentration of bound surface receptors and the dissociation rate, k_{off}.

These processes can be summarized in the following system of partial differential equations

$$\begin{cases} \dfrac{\partial C_F}{\partial t} &= D\nabla^2 C_F &- K_{on}C_F + K_{off}C_B, \\ \dfrac{\partial C_B}{\partial t} &= & K_{on}C_F - K_{off}C_B. \end{cases} \tag{4.4}$$

The binding and dissociation rates are only valid in the region of the PSD and thus become functions of position, that are defined as:

$$\begin{aligned} K_{on}(\boldsymbol{r}) &= \begin{cases} k_{on} & \boldsymbol{r} \in \text{PSD}, \\ 0 & \text{otherwise}. \end{cases} \\ K_{off}(\boldsymbol{r}) &= \begin{cases} k_{off} & \boldsymbol{r} \in \text{PSD}, \\ 0 & \text{otherwise}. \end{cases} \end{aligned} \tag{4.5}$$

4.3.3. INTRODUCING AN EXOCYTIC EVENT

Again, exocytosis occurs at the beginning of a simulation and is therefore implemented as an initial condition. There are some differences with model I however. For the stochastic particle-based model their is no objection in releasing all particles in exactly the same place. This could be seen as an initial condition that takes on the form of a Dirac delta function that is zero everywhere except for the location of exocytosis. The drawback for such an initial condition is that it is very hard to implement in a finite element framework, since the measure of such a location of exocytosis is zero and the function value at this point does not exist. We overcome these challenges by defining a surface, rather than a point, of exocytosis. This surface is typically

a closed, simply connected subspace A_{exo} of our domain of computation, located either on the dendrite or one a spine. The initial condition is then prescribed as follows:

$$\begin{aligned} C_F(\boldsymbol{r},0) &= \begin{cases} c_0 & \boldsymbol{r} \in A_{exo}, \\ 0 & \text{otherwise}, \end{cases} \\ C_B(\boldsymbol{r},0) &= 0 \qquad \text{everywhere}. \end{aligned} \tag{4.6}$$

c_0 is the initial concentration of unbound particles at the region of exocytosis A_{exo}. Also this definition creates implementational difficulties, since the function for $C_F(\boldsymbol{r},0)$ is discontinuous. The way this is dealt with can be found in Appendix C.3.

4.3.4. BOUNDARY CONDITIONS

We would like to model the boundaries as determined in Section 4.1.3. To preserve the cylindrical topology of the dendritic shaft, we impose periodic boundary in the y-direction,

$$C(x,y,t) = C(x,y+2\pi k R_d,t), \qquad \forall k \in \mathbb{Z}. \tag{4.7}$$

To model reflection at the ends at $x = 0$ and $x = l$ we impose homogeneous Neumann boundary conditions,

$$\frac{\partial C}{\partial x}(0,y,t) = \frac{\partial C}{\partial x}(l,y,t) = 0. \tag{4.8}$$

As mentioned, for this model we will only use the variant in which the PSD is modeled as a location where receptors can bind and unbind. Since the interaction between free and bound receptors are modeled by Eq. (4.4), no boundary condition at the interface between PSD and rest of the spine is required.

4.3.5. SIMULATING THE DIFFUSION EQUATION ON A CURVED SURFACE

To numerically solve the system of partial differential equations of Eq. (4.4) with initial conditions given in Eq. (4.6) and boundary conditions in Eqs. (4.7, 4.8), we use a finite element method and a implicit time integration scheme. The details can be found in Appendix C.

4.4. SIMILARITIES AND DIFFERENCES BETWEEN MODEL I AND II

Both models possess their own characteristics. Here we briefly summarize and bundle their similarities and differences.

In the stochastic, particle-based model we are – as the name suggests – able to track the trajectories of individual particles. This allows us to obtain a lot of information out of the system. First passage times are easily computed and by the means of Monte Carlo type methods many statistics can be derived from simulations. Another advantage of this scheme is its flexibility. Complicated boundary conditions are easily implemented, by applying geometric rules. Because the method is not bounded by discretizations in place, new trajectories can be initiated and existing ones can be terminated on any location at any time step.

However, when we would like to assess concentrations of particles at a certain location or time, we need to simulate a lot of particles or average over some time steps so that randomness gets undetectable or confidence intervals get reasonably small. Neglecting the initiation and postprocessing – computation time is proportional to the number of particles, making this model uninviting to simulate concentrations.

Another benefit of the concentration-based model is that it simulates concentration by nature. When we are interested in concentrations, this method is less computationally intensive. When using a implicit method for time integration, this scheme generally handles larger time steps. This model is less flexible, because initial conditions and intermediate solutions have to be sought in the space spanned by the basis functions. This makes it harder to simulate the analog of the release or capture of individual particle(s). Boundary conditions are less easily applied, because they have to be incorporated in the FEM-framework and cannot be applied ad hoc, as in the particle-based model. Furthermore, a different system of partial differential equations has to be solved in order to calculate mean first passage times, which essentially doubles the computation time if this quantity needs to be derived as well. Other moments of first passage times, like the standard deviation, cannot generally be obtained.

5

DESIGN OF TEST CASES

Is this chapter we present the test cases that were used to help answer the research questions described in Chapter 2. The results of the implementation of these test cases are discussed in Chapter 6. All test cases have a similar design. A dendrite of certain length and radius is introduced with two spines attached to it. This setup allows us to explore the influence of the morphology of the spines on the diffusion process.

5.1. DOMAIN OF COMPUTATION

The geometry of the test cases is schematically shown in Figure 5.1. We define a working space of length l and width $w = 2\pi \cdot R_d$, where R_d denotes the radius of the dendrite. This area is populated by two circular geometries modeling the entry of two spines. The centers of these circles are spaced at a distance of a in the x-direction and the radius is denoted by R_{exit}.

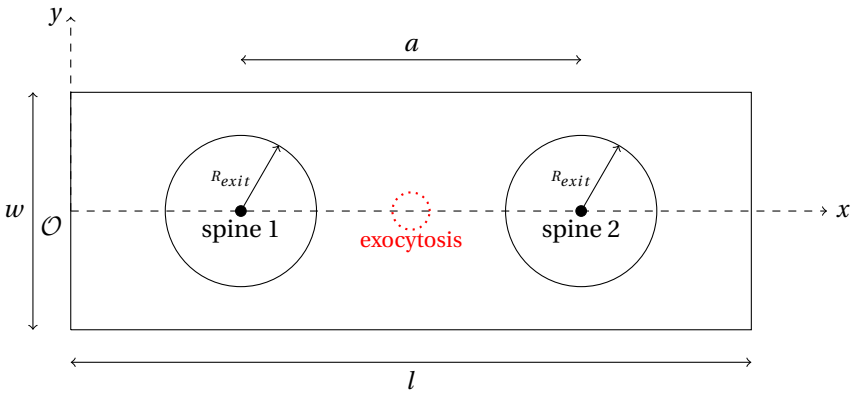

Figure 5.1: Top view of geometry of test cases.

For the morphology of the spines we use the results of [42], as discussed in Section 4.1.1. We use three different morphologies, corresponding to a surface area of A = 1.5, 3.0 and 5.0.

5.1.1. WHAT CONSTITUTES A GOOD COMPARISON BETWEEN SHAPES?

The used spines can be found in Figure 5.2. By construction the size of these three shapes (corresponding to A = 1.5, 3.0 and 5.0) differ significantly. This difference complicates the mutual comparison. Take into mind two spines with the same shape but different size, differing from each other by scaling with a certain factor.

On average, a particle being released on the dendrite (dendritic exocytosis) will take more time to travel to the top of the bigger spine than to the top of the smaller spine. This is, however, not due to a difference in shape, but a difference in size. This demonstrates the difficulty in comparing the influence of the shape on the diffusion process when the size of the spines differ heavily. The question will then always rise: is a measured difference a consequence of shape or of size?

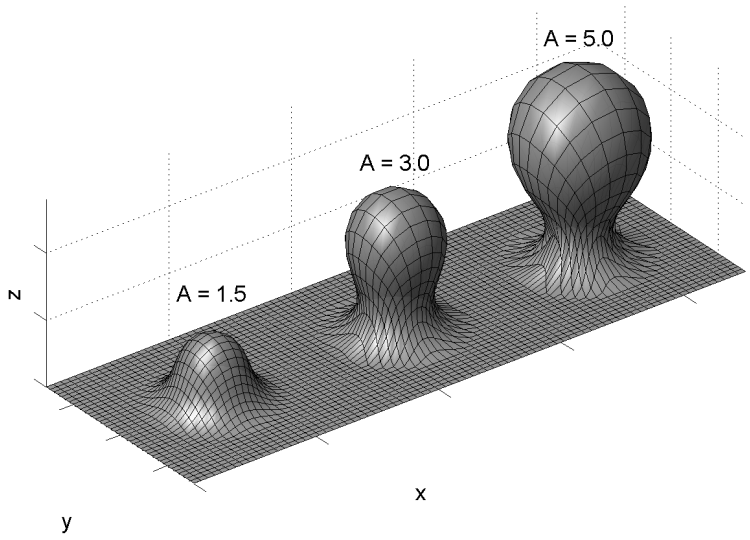

Figure 5.2: Shapes of used spines. A indicates the factor the surface area of the spine has swollen compared to the flat state.

It is clear that we have to compensate for this size difference. A natural way to do this is to assign a scaling factor to each spine to make them comparable. There are multiple ways to define this scaling factor. Straightforward options include:

(i) Equalizing the shortest distance from the dendrite (the plane at the $z = 0$ level);

(ii) Equalizing the out-of-plane surface area.

There is no obvious choice in how to scale the spines. We explain and motivate the choice we made, but the reader should be aware that alternative approaches could also be suitable and might lead to different results.

We choose to rescale the spines in the following way. For each spine a circle is defined on the dendrite with as center the point where the axis of the spine intersects the dendrite and fixed radius. After normalization we fix this radius to 1. We take the surface area of a spine defined by swelling parameter $A = 1.5$ as reference area. Then we scale the other spines down in such a way that the surface area enclosed by the defined circle and the boundary of the postsynaptic density equals the reference area. For clarity, these surfaces are shown in Figure 5.3.

The chosen method is motivated by the following two arguments:

- The circles on the dendrite corresponding to each spine (blue circles in Fig. 5.3) all have the same dimensions. Therefore the probability of a particle reaching such a circle is equivalent for all spines if we ignore boundary effects of the domain and draw from the uniform distribution to determine a starting position of this particle on the dendrite;
- After reaching one of these circles the available surface area between this circle and the postsynaptic density (of which the boundary is depicted with blue circles in Fig. 5.3) is equal for each spine shapes.

From now one we will refer to the surface area of the surfaces between the red and green circle in Fig. 5.3 as the reference surface area, A_{ref}.

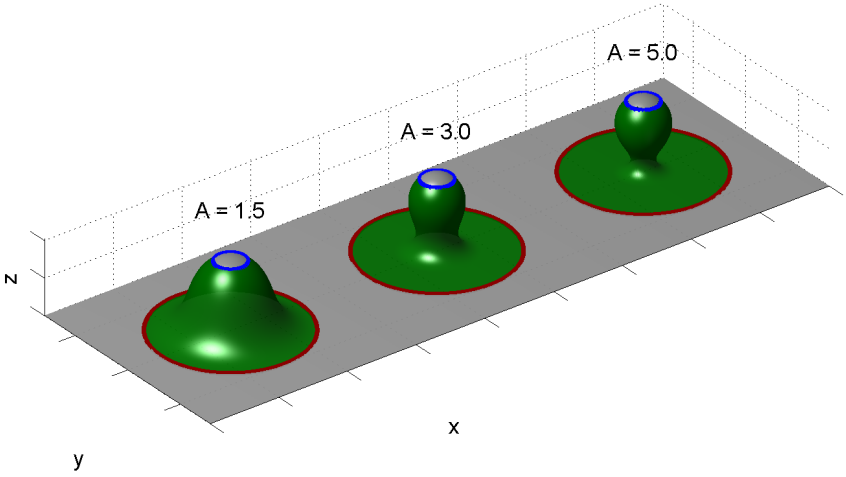

Figure 5.3: Spines after rescaling. The green surfaces have equal surface area.

5.2. THE POSTSYNAPTIC DENSITY

As discussed in Chapter 4, the ongoing binding process at the postsynaptic density is modeled in two ways. The first way is to mimic the binding and unbinding process at the site of the PSD (model I and II), the second way is to treat the boundary of the PSD as an absorbing boundary (model I only).

5.3. EXOCYTOSIS

We would like to assess the influence of shape of a surface on the thereon ongoing diffusion process, but more specifically we would like to determine the differences of spinal and dendritic exocytosis. In order to do this, we designate locations for both types.

5.3.1. DENDRITIC EXOCYTOSIS

In case of dendritic exocytosis, the most straightforward location is on the dendrite, in the middle between the two spines as indicated in Fig. 5.1. For the particle based model we will release all particles at the same point, exactly in the middle at $(x, y) = (l/2, 0)$. For the concentration-based model, we define a disk of exocytosis, A_{exo}, with centre at $(x, y) = (l/2, 0)$.

5.3.2. SPINAL EXOCYTOSIS

In case of spinal exocytosis it is harder to designate a location of exocytosis. We choose to position the location of exocytosis at the height on a spine at which there 10% of the reference surface area, A_{ref}, between this position and the boundary of the PSD (blue in Fig. 5.3) and 90% of A_{ref} between the location of exocytosis and the red circles located on the dendrite as shown in Figure 5.3. This is clarified further in Fig. 5.4.

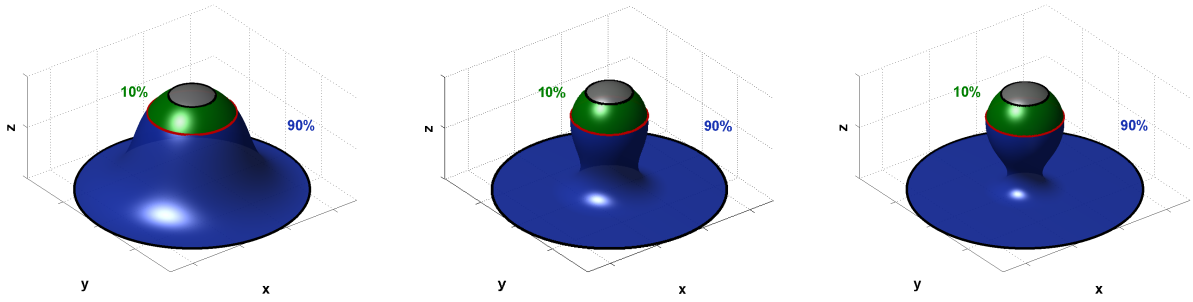

(a) $A = 1.5$. **(b)** $A = 3.0$. **(c)** $A = 5.0$.

Figure 5.4: The green surface has a surface area of 10% of A_{ref} and the blue surface has a surface area of 90% of A_{ref}. The red circle indicates the height of exocytosis and the grey surface represents the PSD.

5.4. CROSSTALK

One of our research questions states:

> What is a measure for the amount of synaptic crosstalk caused by receptor diffusion?

As explained in Section 2.2.3 crosstalk is caused by a spillover of neurotransmitter from one synapse into another synapse (see [32]) or by the lateral diffusion of receptors from a spine to neighboring spines. We focus on the latter one. As opposed to the first version of crosstalk, the second one is not yet quantitatively assessed in literature. This also means that no definition of a measure of synaptic crosstalk caused by receptor diffusion has been given yet. Therefore we define our own procedure to assess the amount of crosstalk, which we base on the following insights:

- The lifetime of the receptors we are regarding (typically AMPA and NMDA receptors) does not allow them to visit a great number of synapses [45]. The receptors can diffuse freely for a limited time until being transported to the intracellular space, where they are disintegrated or transported for exocytosis elsewhere;
- We know from experiments that receptors are exocytosed in stimulated spines and adjacent dendrites [46].

The first insight leads to the following assumption: since the lifetime of a receptor is limited and the number of synapses in which a receptor can reside is constrained, the first PSD it encounters after exocytosis is the most relevant one. Combining this with the experimental result that the release of receptors is targeted on specific spines, we give our definition of a receptor that causes crosstalk in Definition 1.

Definition 1. A receptor that causes crosstalk is a receptor which, after being exocytosed in a specific spine, reaches the PSD of another spine before it reaches the PSD of the spine it was released in.

Now we can define a measure of crosstalk of a certain system or simulation. It is given in Definition 2.

Definition 2. The amount of crosstalk in a certain system is defined by expressing the number of receptors that cause crosstalk by Definition 1 as a percentage of the total number of receptors exocytosed in a specific spine.

The procedure we developed to measure crosstalk can be used with the stochastic particle-based model. In this case we treat the boundaries of the PSDs as absorbing boundaries, since we are only interested in the first PSD a receptor reaches. An exocytic event is created in one of the spines, by initiating trajectories of particles their, we track these particles until they reach the boundary of a PSD. Once it does, it is recorded which PSD

boundary it reached and how long it took to get their. This data will form the basis of the results considering crosstalk.

A flow chart depicting the algorithm can be found in Appendix D.

6

RESULTS

In this chapter we present the results obtained after implementation and running simulations of the particle-based as well as the concentration-based model. We know that exocytosis occurs on the dendrite surface as well as in spines heads [46]. We would like to know what the effect of different locations of exocytosis is on the receptor concentration in spines in the times following this exocytosis. Furthermore, we are interested in what role the morphology of spines play, considering both types of exocytosis.

We subdivide the results in correspondence with these two locations of exocytosis. First we present results of simulations starting from dendritic exocytosis, followed by results of simulations starting with spinal exocytosis. Results from both models are presented in similar simulation setups. An extensive discussion of all outcomes and corresponding conclusions is documented in Chapter 7.

6.1. DENDRITIC EXOCYTOSIS

In this section we present the results of the simulations that were initiated by dendritic exocytosis. We are interested in how the shape of spines alters the temporal evolution of receptor concentration in neighboring spines after dendritic exocytosis.

In these simulations we use the geometry as shown in Fig. 5.1. The precise parameters can be found in Table 6.1. The initial condition represents an exocytic event on the dendrite, in the middle between two spines, i.e. with $(x_0, y_0, z_0) = (2.5, 0, 0)$. For the particle-based model all particles trajectories are initiated at this coordinate. For the concentration-based model a circular region with this coordinate as its centre is defined, in which an increased concentration is defined at the moment of exocytosis. This leads to a situation in which at the time of exocytosis the available surface on both sides from the location of exocytosis is equal. This is clarified in Figure 6.1.

We start with presenting results from simulations in which the postsynaptic density is modeled as an absorbing boundary. This is an simplified version of the model, in which particles that reach the PSD are not longer taken into account for the remainder of the simulation. In reality, however, particles reaching the postsynaptic density can bind to scaffold proteins present in the PSD. In an extension of the model, we incorporate this binding and dissociation process. The results of this version are also discussed.

6.1.1. ABSORPTION AT THE POSTSYNAPTIC DENSITY

Next, we consider the version of the model in which particles reaching the boundary of any PSD are taken out of the system, hence treating this boundary as an absorbing boundary. Since in this version it is possible for particles to leave the system and there is no source term involved, the equilibrium state of this version will be

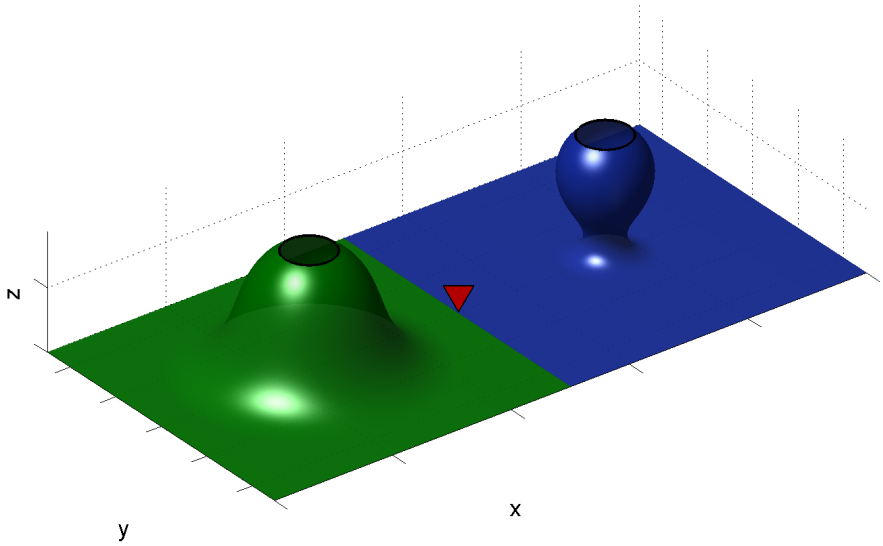

Figure 6.1: In the case of dendritic exocytosis the available surface on both sides of the location of exocytosis is equal. The blue and green colored surfaces have equal surface area. The red triangle indicates the location of exocytosis.

Category	Parameter	Notation	Value	Dimension
Dimensions of geometry	Dendrite width	w	2.5	μm
	Dendrite length	L	5	μm
	Exit radius spine	R_{exit}	1	μm
	Spine spacing	a	2.5	μm
	Radius of PSD	R_{PSD}	0.2	μm
Positions	Exocytic location	(x_0, y_0, z_0)	varying, see text.	μm
Numbers	Number of receptors	N_{part}	10^4 or 10^6	-
Times	Time step	Δt	$2.5 \cdot 10^{-4}$	s
	Duration of simulations	T_{end}	300	s
Diffusion coefficients	Diffusion coefficient	D	0.1	$\mu m^2/s$
Kinetic rates	Receptor binding rate	k_{on}	20	s^{-1}
	Receptor dissociation rate	k_{off}	1	s^{-1}

Table 6.1: Model parameters for simulations.

an empty system – the trivial solution. This implementation is used to keep track of which PSD each particles encounters first and how long they need to do so. With this information we can calculate an estimate for the mean first passage time (MFPT) and thereby study how different compositions of geometry influence this statistic. This feature is unique to the particle-based model and therefore this version is only implemented in that model.

In a system of two spines with dendritic exocytosis, we have a conditional mean first passage time for the boundary of the PSD of the left spine and another conditional mean first passage time for the boundary of the PSD of the right spine. We present a formal definition of these conditional first passage times.

Definition 3. Let $\boldsymbol{X}_t$ be the stochastic process, which represents the diffusion of a single particle. Let $E_1 \subset \Omega$ be a subset of our domain of computation Ω. Then the first passage time τ_{E_1} is the random variable defined by

$$\tau_{E_1} := \inf\{t > 0 | \boldsymbol{X}_t \in E_1\}.$$

Let $E_2 \subset \Omega$ another subset of Ω satisfying $E_1 \cap E_2 = \emptyset$. The conditional first passage time $\tau\left(E_1 | E_2^c\right)$ is the first

passage time to E_1, given no earlier visit to E_2. These conditional first passage times have been studied in [50].

The conditional mean first passage time for the postsynaptic density of the left spine is defined as

$$\mu_{FPT}^{left} = \mathbb{E}\left[\tau\left(PSD_{left} \quad | \quad PSD_{right}^{C} \right) \right].$$

μ_{FPT}^{right} is defined similarly. Clearly, these statistics depend upon the location of exocytosis and the chosen composition of spines. We will use these statistics as an indication of how long it takes on average for a receptor to reach a certain postsynaptic density, given that that is the first postsynaptic density it encounters.

We can calculate estimates for this statistic using a Monte Carlo type approach. After simulating the exocytic event, simulations were run until all particles left the system through either the absorbing boundary in the left or right spine. Each particle serves as a realization in the Monte Carlo method. Per realization the exit location (the absorbing boundary in either of the spines) and the exit time are recorded. From the results of this simulation sample mean and sample standard deviations can be calculated, including there respective confidence intervals. The overall MFPT is denoted by μ_{FPT} and its (unbiased) estimator, the sample mean with $\hat{\mu}_{FPT}$. The standard deviation of the MFPT is denoted with σ_{FPT} and its (unbiased) estimator, the sample standard deviation, with $\hat{\sigma}_{FPT}$. A similar and intuitive notation is used for the conditional mean first passage times, as given in Table 6.2.

$\mu_{FPT}^{left}, \mu_{FPT}^{right}$	MFPT of particles exiting from left or right spine;
$\hat{\mu}_{FPT}^{left}, \hat{\mu}_{FPT}^{right}$	corresponding sample mean;
$\sigma_{FPT}^{left}, \sigma_{FPT}^{right}$	standard deviation of MFPT of particles exiting from left or right spine;
$\hat{\sigma}_{FPT}^{left}, \hat{\sigma}_{FPT}^{right}$	corresponding sample standard deviation.

Table 6.2: Notation for used mean first passage time, its standard deviation and their corresponding estimators.

Simulations start with dendritic exocytosis and boundaries of the PSDs are treated as absorbing boundaries. Furthermore, parameters are as in Table 6.1, with the number of particles equal to 10^6. The reason for this higher number is that we are performing a Monte Carlo type simulation and an higher number of realizations will narrow our confidence intervals.

Two equally shaped spines. We begin with looking look at the results of experiments in which the left and right spine have the same shape as schematically shown in Figure 6.2.

Except from the statistics from Table 6.2, we can use the experimentally obtained first passage times to calculate an empirical probability density function (EPDF) for the mean first passage time. A plot of the EPDFs for these simulations can be found in Figure 6.3. In Fig. 6.3a the axis are linearly scaled and in Fig. 6.3b the y-axis has a logarithmic scale.

Since in these test cases the left and right spine have identical shapes and we simulate an exocytosis on the dendrite in the middle between them, we know that

$$\mu_{FPT}^{left} \sim \mu_{FPT}^{right},$$

where $\sim$ indicates that the statistical distributions of the two variables are the same. An estimate for the conditional mean first passage time and its standard deviation are given in Table 6.3. We also present 95% confidence intervals.

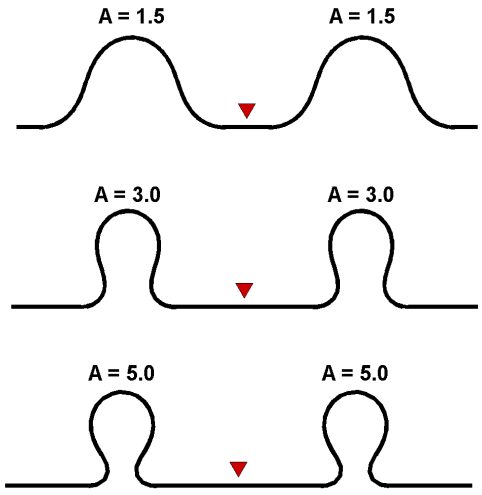

Figure 6.2: Schematic diagram of dendritic exocytosis with two spines having matching shape. The red triangle indicates the location of exocytosis.

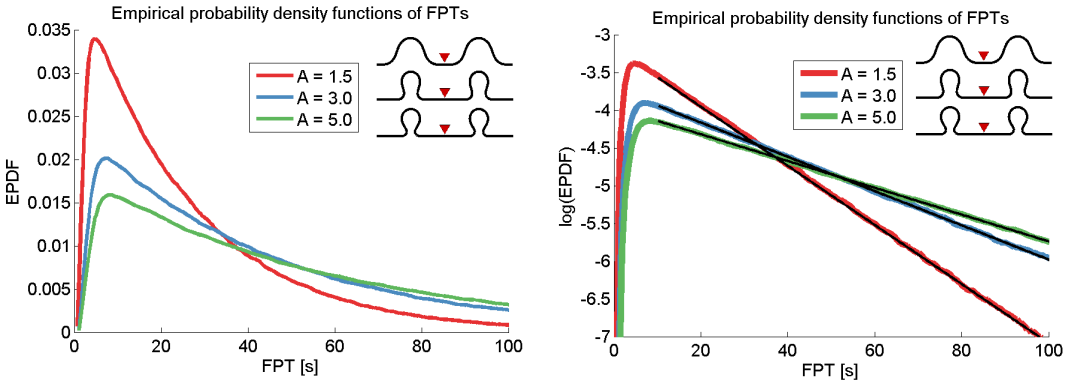

(a) **(b)**

Figure 6.3: EPDFs of simulations with dendritic exocytosis, where left and right spine have same shape.

Shape parameter	$\hat{\mu}^{l/r}_{FPT}[s]$	95% C.I.	$\hat{\sigma}^{l/r}_{FPT}$ [s]	[95% C.I.]
$A = 1.5$	27.603	± 0.050	25.459	[25.423, 25.494]
$A = 3.0$	47.292	± 0.086	44.110	[44.049, 44, 172]
$A = 5.0$	59.990	± 0.111	56.446	[56.368, 56.524]

Table 6.3: Sample mean and sample standard deviation of conditional mean first passage times for dendritic exocytosis of 10^6 particles in the middle between two spines with identical shape. The intervals given are 95% confidence intervals.

From Table 6.3 and Figure 6.3 we conclude that after exocytosis on the dendrite the time a receptor needs to reach a postsynaptic density increases significantly when the shape parameter A increases. In other words, after exocytosis on the dendrite a receptor reaches a PSD of a stubby spine faster than a mushroom shaped spine.

Two differently shaped spines. A logical next step is to quantitatively assess how these statistics change when the morphology of the left and right shape differ from each other and what portion of the receptors reach the postsynaptic density of the left and right spine in that case. We run experiments with dendritic exocytosis and two spines, with different morphology, as schematically shown in Figure 6.4.

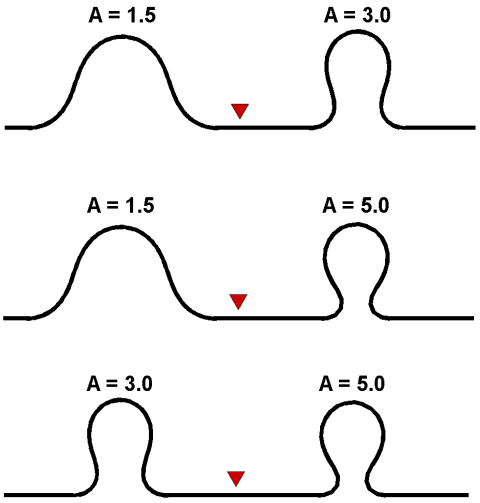

Figure 6.4: Schematic diagram of dendritic exocytosis with two spines having different shape. The red triangle indicates the location of exocytosis.

Cond. MFPT for: / In combination with:	$A = 1.5$		$A = 3.0$		$A = 5.0$	
	$\hat{\mu}_{FPT}^{cond}[s]$	95% C.I.	$\hat{\mu}_{FPT}^{cond}[s]$	95% C.I.	$\hat{\mu}_{FPT}^{cond}[s]$	95% C.I.
$A = 1.5$	27.603	±0.050	38.330	±0.105	43.457	±0.125
$A = 3.0$	34.050	±0.085	47.292	±0.086	54.044	±0.145
$A = 5.0$	37.569	±0.092	52.255	±0.132	59.990	±0.111

Table 6.4: Sample mean of conditional mean first passage times for dendritic exocytosis of 10^6 particles in the middle between two spines with different shape. The intervals given are 95% confidence intervals.

$\hat{\sigma}_{FPT}^{cond}$: / Comb. w.:	$A = 1.5$		$A = 3.0$		$A = 5.0$	
	$\hat{\sigma}_{FPT}^{cond}$ [s]	[95% C.I.]	$\hat{\sigma}_{FPT}^{cond}$ [s]	[95% C.I.]	$\hat{\sigma}_{FPT}^{cond}$ [s]	[95% C.I.]
$A = 1.5$	25.459	[25.423, 25.494]	34.551	[34.476, 34.625]	39.069	[38.981, 39.158]
$A = 3.0$	33.108	[33.048, 33.168]	44.110	[44.049, 44, 172]	50.076	[49.974, 50.179]
$A = 5.0$	37.209	[37.143, 37.274]	49.541	[49.448, 49.634]	56.446	[56.368, 56.524]

Table 6.5: Sample standard deviation of conditional mean first passage times for dendritic exocytosis of 10^6 particles in the middle between two spines with different shape. The intervals given are 95% confidence intervals.

An estimate for the conditional mean first passage time and its standard deviation are given in Tables 6.4 and 6.5. We also present 95% confidence intervals.

From Table 6.4 we conclude that the conditional mean first passage times of a PSD of a certain spine changes in a particular way when the two spines in the system do not have equal shape. In a system of two differently shaped spines the conditional mean first passage time of the spine corresponding to a smaller value of shape parameter A is still lower than the spine corresponding to a higher value of A, but the differences have become smaller. To easily observe this, we have included the values for μ_{FPT}^{cond} when left and right spine are equally shaped in Tab. 6.4. This result is visualized in Figure 6.5.

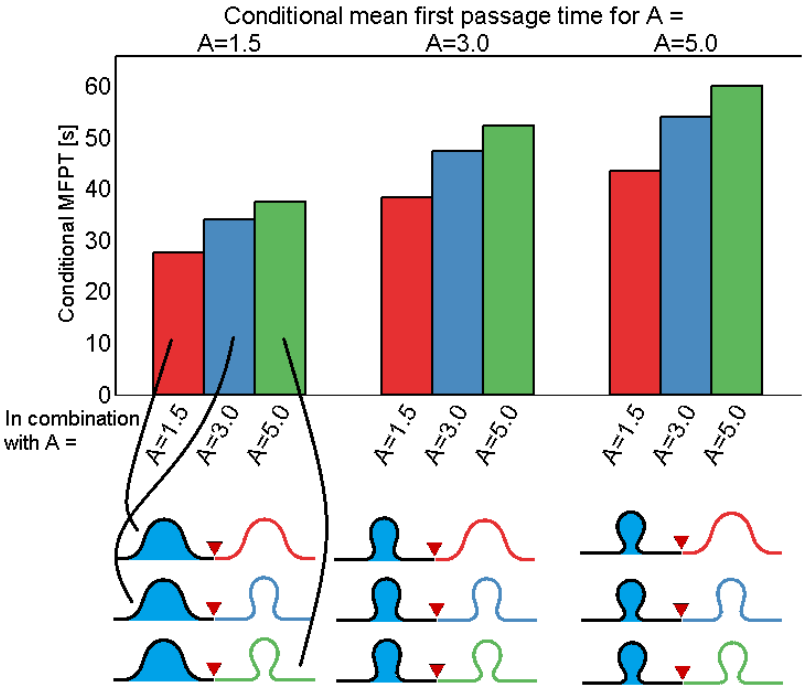

Figure 6.5: Conditional mean first passage times. The conditional mean first passage times correspond to the values of A listed at the top of the graph. The values listed at the bottom of the graph represent the value of A with which the initial spine was combined. This is explained by the schematic diagrams of the different experiments below the plot.

From Table 6.4, we can draw an interesting conclusion. In the case of dendritic exocytosis, the conditional mean first passage time from the location of exocytosis to the boundary of a specific PSD does not only depend on the morphology of the associated spine, but also on the morphology of its neighboring spines. Moreover, this effect is significant, as can be seen from Figure 6.5.

A similar observation can be done while considering the standard deviation of the mean first passage times as presented in Tab. 6.5.

6.1.2. TRAPPING AT THE POSTSYNAPTIC DENSITY

As discussed in Section 4.1.4, the PSD is modeled in two ways. First we consider the version of the model in which trapping at the PSD is incorporated. In this version particles cannot leave the system and therefore the model has a non trivial equilibrium solution. Since neurotransmitter receptors have a limited lifetime, time scales involved in reaching an equilibrium situation are particularly relevant. Therefore we consider both equilibrium state as well as the behavior of the system towards this equilibrium.

In the particle based model, we release a number of 10^4 particles at $t = 0$. Even though the number of particles is high, for the particle-based model every simulation of 10^4 particles will be different due to random fluctuations. It is important to assess the proportions of these fluctuations. We run 10 simulations, with each a release of 10^4 particles on the dendrite, it the middle between two spines. One spine has shape parameter $A = 1.5$ and the other shape parameter $A = 5.0$. We calculate the concentration in the PSD and take the mean of these 10 simulations. We also calculate 95% confidence intervals for our simulations. The result can be found in Figure 6.6. From here on, we will present the mean of these 10 simulations, unless indicated otherwise.

Simulations start with dendritic exocytosis and the PSDs are treated as regions at which a binding an dissociation process takes place. Parameters are as in Table 6.1, with $N_{part} = 10^4$ and $T_{end} = 300s$. To get an insight in how the simulation is performed, we have included movie A1 for the particle-based model and movie A3

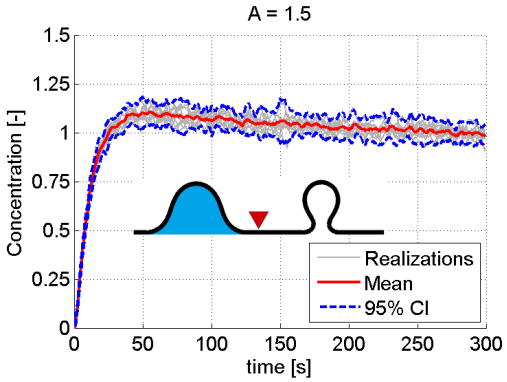

(a) Concentration of free particles in PSD. $A = 1.5$.

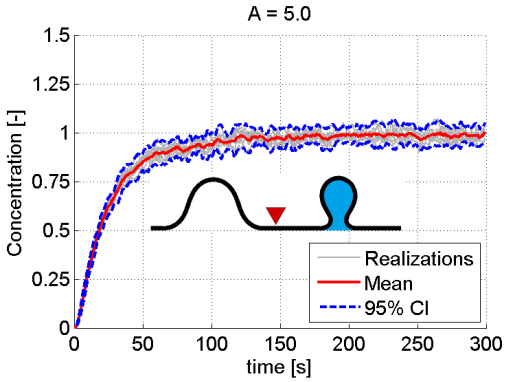

(b) Concentration of free particles in PSD. $A = 5.0$.

Figure 6.6: Concentration of particles in the postsynaptic density over time after dendritic exocytosis in the middle between two spines, one with shape parameter $A = 1.5$ (a), and one with shape parameter $A = 5.0$ (b).

for the concentration-based model, see Appendix A.

To analyze the results, we begin with investigating the typical time scales it takes to reach equilibrium. To do this, the concentration of particles in the postsynaptic density of both spines is recorded over time. Since in this version of our model trapping and dissociation at the PSD is possible, both the concentration of bound and free particles is computed. We have normalized the concentration of particles by dividing by the uniform concentration $c_{uniform}$, which is for model I defined as

$$c_{uniform} = \frac{\text{Total number of particles in system}}{\text{Total available surface area}} = \frac{N_{part}}{A_{total}}. \tag{6.1}$$

For model II, $c_{uniform}$ is defined as

$$c_{uniform} = \frac{\text{Total amount of receptors in system}}{\text{Total available surface area}} = \frac{\int_\Omega C(\boldsymbol{r}, t)\, \mathrm{d}\Omega}{\int_\Omega \mathrm{d}\Omega}. \tag{6.2}$$

This way of normalization (6.1) implies that an homogeneous concentration everywhere on the domain would be indicated with a normalized concentration of one everywhere.

The normalized concentration at the PSD of both spines over time is plotted for different compositions of geometries in Figure 6.7. Reults for both models are shown. We show results for a composition of two spines with shape parameter $A = 1.5$, for free (Fig. 6.7a) and bound (Fig. 6.7b) particles at the PSD. In Fig. 6.7c and 6.7d the concentration for free particles at the PSD is plotted for a combination of a geometry characterized by $A = 1.5$ for spine 1 and $A = 3.0$ and $A = 5.0$ for spine 2 respectively. From these plots we make a few observations:

- For larger A, the time needed to reach equilibrium gets larger as well;
- For larger A the concentration towards equilibrium is lower than for smaller A;
- The geometry does not influence the equilibrium concentration itself, merely the timescales in concentration towards this equilibrium.

In Figure 6.7 we see an overshoot in the concentration at the PSD of spine with shape parameter $A = 1.5$. It is detected easily in Figs. 6.7c and 6.7d, but is also present in the other figures. The overshoot is more prominent in the results of the concentration-based model. We expect this overshoot to happen for shapes that resemble the flat state, since it would also occur when releasing a certain concentration on a flat surface and measuring the concentration at a certain location in that neighborhood over time.

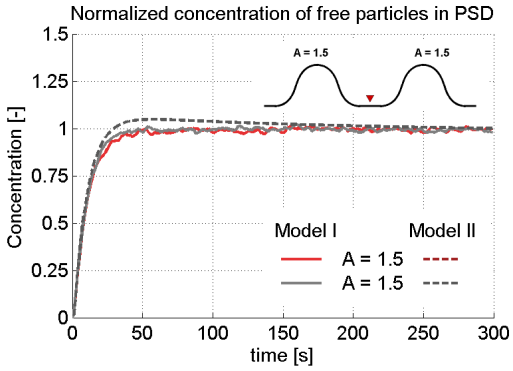

(a) Concentration of free particles in PSD. The geometry of the two spines is identical ($A = 1.5$). The red and grey dashed line coincide, causing the red dashed line to be invisible.

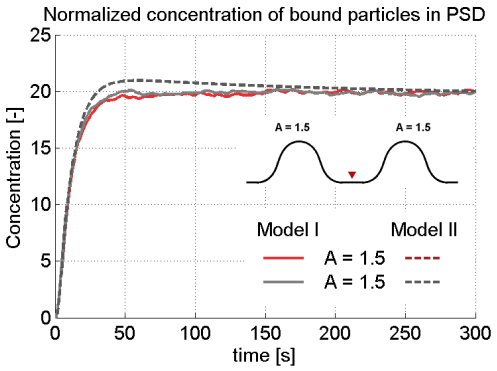

(b) Concentration of bound particles in PSD. The geometry of the two spines is identical ($A = 1.5$). The red and grey dashed line coincide, causing the red dashed line to be invisible.

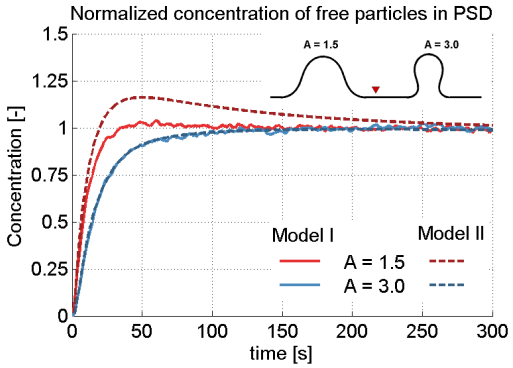

(c) Concentration of free particles in PSD. The geometry of spine 1 is characterized by $A = 1.5$ and the geometry of spine 2 is characterized by $A = 3.0$.

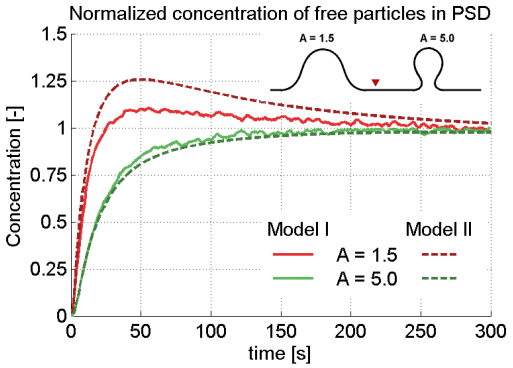

(d) Concentration of free particles in PSD. The geometry of spine 1 is characterized by $A = 1.5$ and the geometry of spine 2 is characterized by $A = 5.0$.

Figure 6.7: Concentration of particles in the postsynaptic density over time after dendritic exocytosis in the middle between two spines. For Figure (a) and (b) the two spines have identical geometry (both $A = 1.5$). In (a) the concentration of free particles is displayed and in (b) the concentration of bound particles is displayed. For (c) and (d) the concentration of free particles is given and the geometry for spine 1 is characterized by $A = 1.5$ and the geometry for spine 2 is characterized by $A = 3.0$ and $A = 5.0$ respectively. The black dash-dot line represents the uniform concentration as computed by Eq. (6.1).

Correspondence of the two models. Although the two models intend to simulate the same diffusion process, their origin and the way they are established differ significantly. From Figure 6.7 we see a strong correspondence between the stochastic particle-based model and the concentration based model, but also some differences. The first thing we would like to point out, is that the slope of the concentrations at the beginning of the simulations coincide excellently. This is a good indication that both models indeed represent the same diffusion process. We also see, however, that the overshoot is not represented in the results in the same way. This overshoot is more prominent in the results of the concentration-based model. We cannot explain this difference, but the explanation most likely has to be sought in the subtle differences between the implementation of model I and II of the binding and unbinding process at the PSD. Overall, the correspondence is a good indication that both models are able to model the initialization phase acceptably well. Moreover, the time scales in concentration are quantitatively equal for the results of both models. A a comprehensive comparison of both models can be found in Section 7.2.2.

The models allow for computing the concentration not only in the PSD of both spines, but also in other areas of the domain of computation. We would like to investigate the concentration along the shaft of the dendrites. Therefore we plot the concentration as a function of surface area from the top of each spine for different points in time. In other words, for fixed moments in time, we measure the concentration of receptors along the shaft, see Figure 6.8. From this figure, it can be seen that we measure the concentration along the

shaft from the top until the base ring. For spines corresponding to a value of A that is larger than 1.5 this means that a part of this area is located on the dendrite.

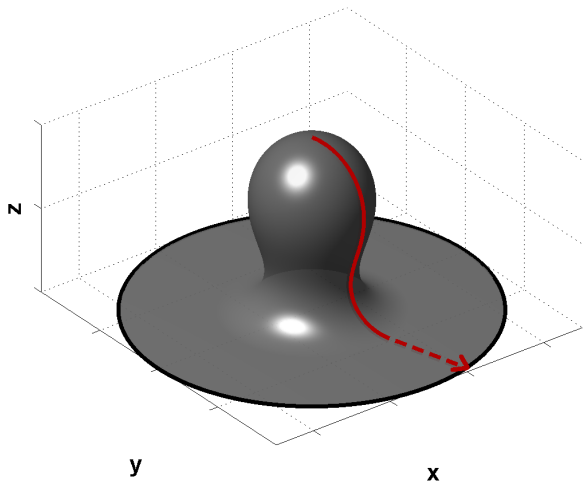

Figure 6.8: We measure the concentration along the shaft as a function of surface area from the top of each spine until the base ring (black). For some spines this means that part of this region lies on the dendrite (striped red line).

In Figure 6.9 the concentration along the shaft is plotted for four time instances after exocytosis. The results are obtained using the particle-based model. We use a domain with two spines corresponding to $A = 1.5$ (stubby) and $A = 5.0$ (mushroom). In these plots the uniform concentration as defined by Eq. (6.1) is indicated with a black dash-dot line in each plot. As mentioned, for the spine corresponding to $A = 5.0$ a large portion of the surface area in which we measure the concentration is located outside the spine, on the dendrite. For clarity, the location of the neck of this spine is indicated in the figures.

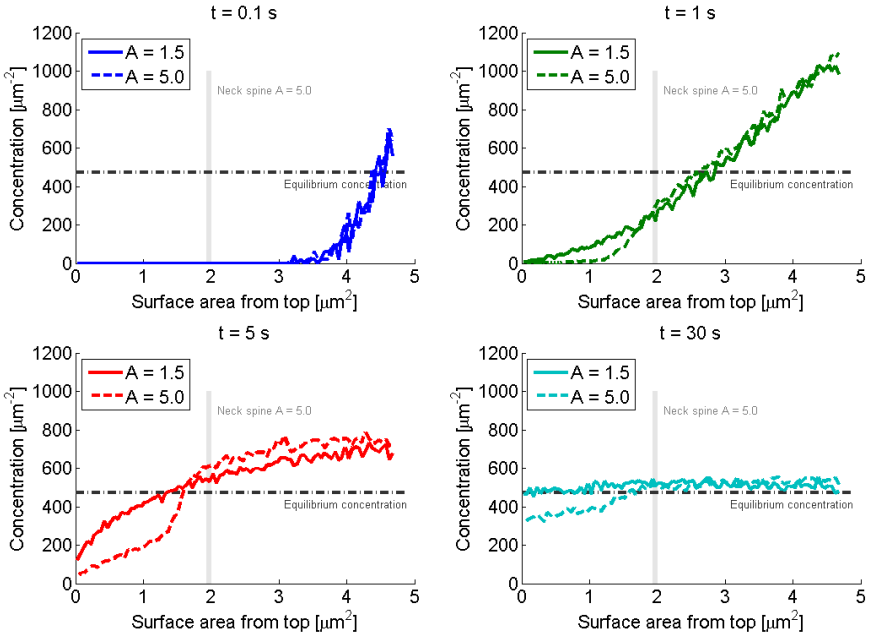

Figure 6.9: Concentration along the shafts of two spines after dendritic exocytosis for four time instances. The elapsed time after exocytosis is indicated above each plot. The uniform concentration is indicated with the black dash-dot line. The location of the neck of the spine corresponding to $A = 5.0$ is indicated with a grey vertical line.

We focus on the part of both spines that is out of the $z = 0$ plane, hence not on the dendrite. The surface area of spine 2 that is out of plane amounts to approximately $1.97\mu m^2$, also indicated in the plots of Fig. 6.9. We can see that in this region the concentration along the shaft inside the dendrite is higher in the stubby spine ($A = 1.5$) than in the mushroom spine ($A = 5$). We conclude that after dendritic exocytosis the timescale involved in equilibration of the concentration of receptors is larger for mushroom-shaped spines as compared to stubby spines.

The concentration-based model is run with the same configuration of spines ($A = 1.5$ and $A = 5.0$). In Figure 6.10 surface plots of the domain are shown and the concentration is indicated using different colors as indicated by the colorbar. We have plotted both the concentration of bound as well as free particles for the same time instances as used for Fig. 6.9. Note that a logarithmic scale is used for the colorbar for the free particles (C_F) and that scales are different for bound and free particles.

We can see from the surface plot of the concentration of free particles (Fig. 6.10a, $10s$ and $30s$) that the concentration in the mushroom shaped spine increases on a longer time scale than concentration in the stubby spine.

From these results we conclude that stubby spines are favored in the case of dendritic exocytosis. In the initialization phase, before reaching equilibrium, the concentration of particles in the spine shaft and at the PSD of stubby spines is higher than for mushroom spines. However, after dendritic exocytosis, concentration rapidly rises in all neighboring spines. In the next section we investigate the effect of spinal exocytosis.

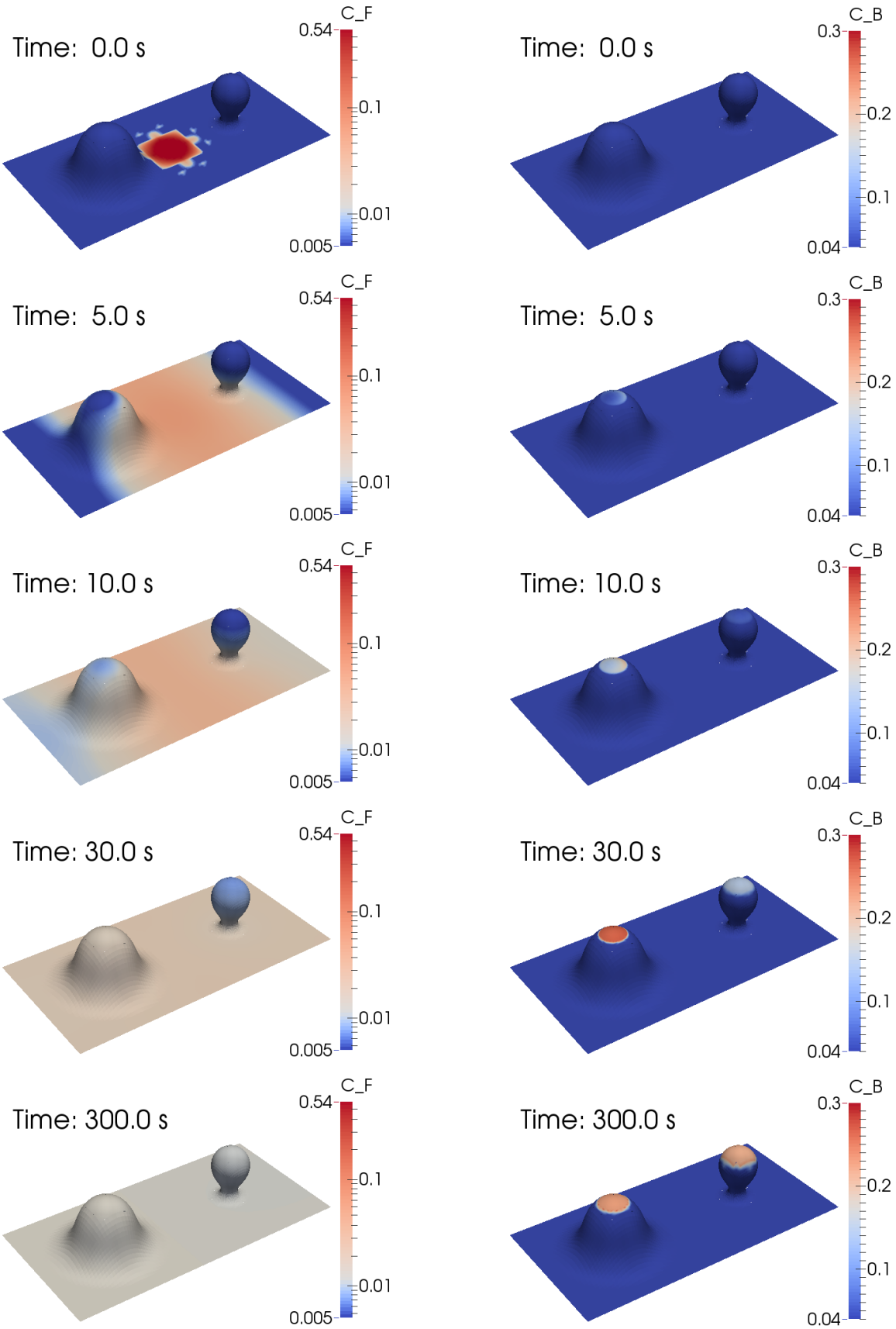

(a) Concentration of free particles, C_F.

(b) Concentration of bound particles, C_B.

Figure 6.10: Concentration of free and bound particles as simulated by the concentration-based model for different time instance. Simulation was initiated with dendritic exocytosis, as can been seen in the top left figure.

6.2. SPINAL EXOCYTOSIS

In this section we present the results of simulations in which the location of exocytosis is changed to a location one of the two spines. The geometry and the setup stays otherwise the same and parameters can again be found in Table 6.1.

We choose the height of the exocytosis in such a way that 10% of the reference surface area, A_{ref} (indicated in green in Fig. 5.3), is between the location of exocytosis and the boundary of the PSD (blue in Fig. 5.3) and 90% of this reference surface area is between the location of exocytosis and the base circle (red in Fig. 5.3). This is clarified in Figure 6.11. Note that the exact location of exocytosis is shape dependent. An exocytosis on this height is simulated by releasing particles uniformly distributed along the ring that is on this height, indicated in red in Fig. 6.11.

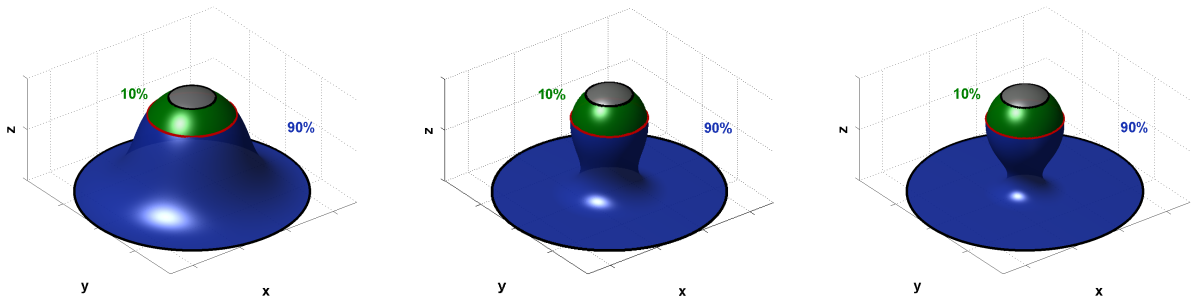

(a) $A = 1.5$. **(b)** $A = 3.0$. **(c)** $A = 5.0$.

Figure 6.11: The green surface has a surface area of 10% of A_{ref} and the blue surface has a surface area of 90% of A_{ref}. The red circle indicates the height of exocytosis and the grey surface represents the PSD.

We start with results from the version of the model in which the boundary of the PSD is modeled as an absorbing boundary, followed by the extension in which the binding and unbinding process at the PSD is taken into account.

6.2.1. ABSORPTION AT THE POSTSYNAPTIC DENSITY

We consider the setup of the model in which we have spinal exocytosis, where particles reaching the boundary of any PSD are taken out of the system. As explained in Section 6.1.1, this setup can be used to calculate (conditional) mean first passage times. Moreover, we use this setup to answer our research question:

How does the morphology of dendritic spines influence the synaptic crosstalk?

We defined a measure for the amount of crosstalk in Definitions 1 and 2. The amount of crosstalk will depend on what shapes of spines are present in the system and in which the exocytosis occurs. After setting up a simulation and initiating an exocytosis in one spine, we record what portion of the 10^6 trajectories of the exocytosed receptors terminate in the PSD of the other spine. The obtained percentages can be found in Table 6.6. We will normalize these percentages by dividing by the reference situation in which both spines have shape parameter $A = 1.5$. In this case the amount of crosstalk is 8.98%. These normalized values for crosstalk can be found in Table 6.7.

From Table 6.7 we conclude that the amount of crosstalk decreases when spines with an higher shape parameter A are in the system. In other words, the more a spine becomes mushroom-shaped, the less crosstalk we observe. A remarkable result is that the amount of crosstalk also decreases when a stubby spine is replaced by a mushroom shaped spine when this is *not* the spine in which exocytosis occurred. This is a good indication that spine morphology at least partially governs spine compartmentalization in two directions. Firstly, after a spinal exocytosis in a mushroom-shaped spine, the elevated concentration will be maintained longer. Secondly, after dendritic exocytosis, the concentration in mushroom-shaped spines will be relatively lower in the

Other spine \ Spine of exocytosis	$A = 1.5$	$A = 3.0$	$A = 5.0$
$A = 1.5$	8.98%	7.48%	6.76%
$A = 3.0$	8.43%	7.22%	6.62%
$A = 5.0$	7.53%	6.61%	6.05%

Table 6.6: Amount of crosstalk for several combinations of spines.

Other spine \ Spine of exocytosis	$A = 1.5$	$A = 3.0$	$A = 5.0$
$A = 1.5$	1.00	0.83	0.75
$A = 3.0$	0.94	0.80	0.74
$A = 5.0$	0.84	0.74	0.67

Table 6.7: Normalized amount of crosstalk for several combinations of spines. Normalized by dividing by amount of crosstalk in reference situation.

initialization phase. The typical mushroom shape of spines enables the spine head to function as a separate component from the rest of the dendrite in the process of lateral diffusion of membrane receptors.

To take a closer look at the influence of shape, in our case determined by shape parameter A, we focus at the marked cells of Table 6.7. These are the cells that correspond to experiments in which both spines have equal shape. To get more data points, we also ran this simulation for other values of A. The result is plotted in Figure 6.12.

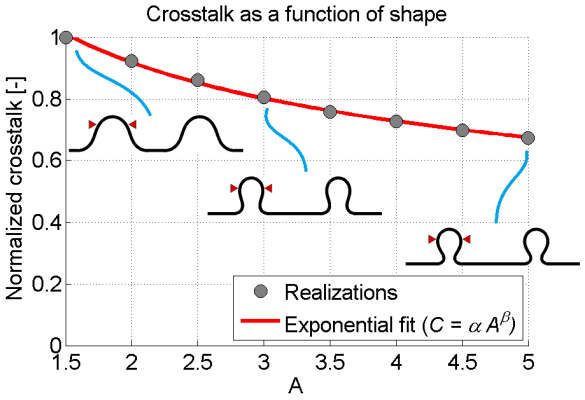

Figure 6.12: Crosstalk as a function of shape parameter in a system in which both spines have equal shape. Data is normalized by dividing values by crosstalk of reference situation. Red line is exponential shape, however range of data is not big enough to properly assess the quality of this fit.

6.2.2. TRAPPING AT THE POSTSYNAPTIC DENSITY

We look at the extension of our models in which the postsynaptic density is modeled as a location at which binding and dissociation of receptors occurs.

For analyzing the results we used the normalization procedure as described in Section 6.1.2 using Eqs. (6.1) and (6.2).

Since we are looking at spinal exocytosis now, we have to specify both which spines are used in the system and in which spine the exocytosis takes place. Simulating all possible combinations gives us a database of 9 simulation results, as indicated in Table 6.8. Here, we discuss the simulations indicated in grey in Table 6.8.

Simulations start with spinal exocytosis and boundaries PSDs are treated as regions where a binding and dissociation process takes place. To get an insight in the type of simulations we perform, we have included

Spine of exocytosis \ Other spine	$A = 1.5$	$A = 3.0$	$A = 1.5$
$A = 1.5$			
$A = 3.0$			
$A = 5.0$			

Table 6.8: Table of possible simulation combination for spinal exocytosis. The number of possible combinations is nine in our setting.

movie A2a and A2b, see Appendix A.

In the particle based model a number of 10^4 particles is released at $t = 0$. The total simulated time is $T_{end} = 300s$. The normalized concentration at the PSD for both spines is plotted in Figure 6.13. In Fig. 6.13a and 6.13b the results are shown for two spines with shape parameter $A = 1.5$. The concentration of free and bound particles are plotted respectively. We see that an equilibrium is reached after approximately 150 seconds.

In Fig. 6.13c and 6.13d the concentration of free particles at the PSD is plotted for two spines with shape parameter $A = 3.0$ and two spines with shape parameter $A = 5.0$ respectively. The time to reach equilibrium increases as A increases. For $A = 3.0$ the time it takes to reach equilibrium is approximately 220 seconds and for $A = 5.0$ approximately 270 seconds. Comparing these plots to the plots of Figure 6.7, we make a few observations:

- In the case of spinal exocytosis, the time needed to reach equilibrium is larger than in the case of dendritic exocytosis;
- Also in the case of spinal exocytosis, the time needed to reach equilibrium is larger for larger values of A.

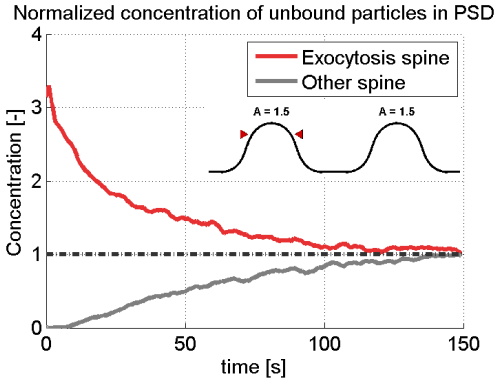

(a) Concentration of free particles in PSD. The geometry of the two spines is identical ($A = 1.5$).

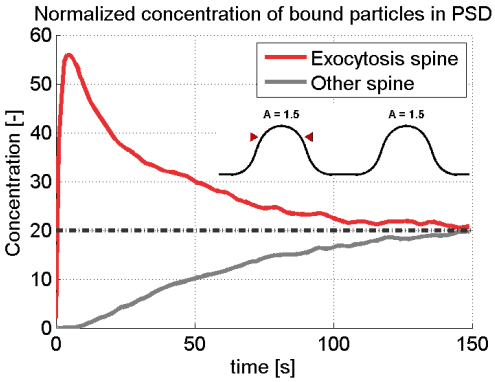

(b) Concentration of bound particles in PSD. The geometry of the two spines is identical ($A = 1.5$).

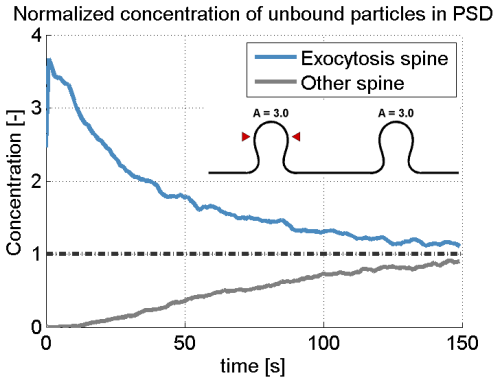

(c) Concentration of bound particles in PSD. The geometry of the two spines is identical ($A = 3.0$).

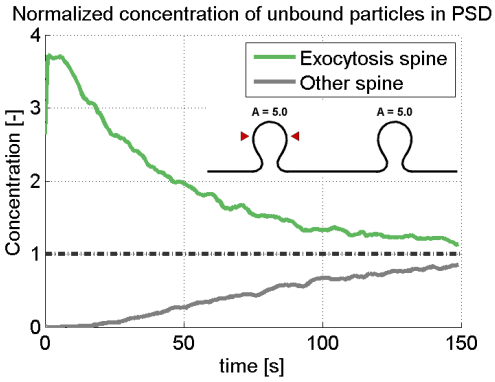

(d) Concentration of bound particles in PSD. The geometry of the two spines is identical ($A = 5.0$).

Figure 6.13: Concentration of particles in the postsynaptic density over time after spinal exocytosis in one of the two spines. For all figures the left and right spine have identical shape. For Figure (a) and (b) the two spines have geometry corresponding to $A = 1.5$. In (a) the concentration of free particles is displayed and in (b) the concentration of bound particles is displayed. In (c) and (d) the concentration of free particles in the PSD for two spines with geometry $A = 3.0$ and $A = 5.0$ is plotted respectively. The black dash-dot line represents the uniform concentration as computed by Eq. (6.1).

7

CONCLUSIONS AND DISCUSSION

7.1. CONCLUSIONS

In this research we designed two models to assess the influence of spine morphology on a lateral diffusion process defined on its surface. With the aid of these models we tried to get insight to what extent spine morphology affects interspinal crosstalk.

Spine morphology is variable and has been classified into different types, based on their appearance: stubby, filopodia, thin and mushroom-shaped [23]. In order to investigate the impact of these typical shapes on the diffusion process, its associated time-scales and crosstalk, we had to capture these geometries in a (mathematical) framework. We did this using the results of [42]. We will discuss this choice in the next section.

By use of the particle-based model, we have shown that as the morphology of spines propagates toward a mushroom shape, the level of crosstalk decreases. This result is obtained both when exocytosis occurs in this mushrooms-shaped spine as well as when it occurs in an other, neighboring, spine (see Chapter 6, Table 6.7 and Figure 6.12). This invigorates the assumption of spine morphology not only governing electrical compartmentalization as discussed in Section 2.1.3 and in [17], but also compartmentalizes the diffusion of surface receptors, as suggested in Section 2.2.1.

Analysis of simulations run with both models shows that dendritic exocytosis increases the receptor concentration in all neighboring spines, but is most beneficial for stubby-shaped spines. In case of dendritic exocytosis, before reaching an equilibrium, receptor concentration is significantly higher in stubby-shaped spines, than in more mushroom-shaped spines (see Chapter 6, Figures 6.7, 6.9 and 6.10). Furthermore, the MFPT for receptors to reach a PSD is notably lower in the case of a system with merely stubby spines than in a system with mushroom-shaped spines (Figure 6.3 and Table 6.3). This result carries over to a system with spines of different shape: also in a domain composed of various shaped spines, the MFPT for receptors to reach a stubby spine is lower, although the differences between shapes decrease (Table 6.4 and Figure 6.5). So, the conditional MFPT from the location of exocytosis to the boundary of a specific PSD does not only depend on the morphology of the associated spine, but also on the morphology of neighboring spines.

Concerning the methodologies used, for both models we solve a diffusion problem on a curved surface. This causes different challenges. We need the Laplace-Beltrami operator to account not only for spatial changes in the solution, but also for spatial changes in the geometry. For the particle-based model we took the curvature of the surface into account by calculating a second order approximation. For the concentration-based model we have to take derivatives of our geometry. The set up of our models differ significantly, but they should model the same diffusion process.

We conclude that both models produce qualitatively comparable results regarding concentration of particles as shown in Figure 6.7. By nature, the stochastic particle-based model shows stochastic fluctuation when

presenting concentration results on specific locations and times. These fluctuations become undetectable when averaging over a large number of particles or time steps, but the consequence of such solutions is compromising on computational aspects such as computation time and memory usage. The results produced by the concentration-based model appear as a good estimate for the mean of the stochastic particle-based model and can be used as such, without the need of increasing the number of particles or averaging over time steps. At the beginning of the initialization phase, we see that the slopes of the concentrations coincide. This is a good indication that both models indeed represent the same diffusion process. We also see, however, that the overshoot is not represented in the results in the same way. We cannot explain this difference, but the explanation most likely has to be sought in the subtle differences between the implementation of model I and II of the binding and unbinding process at the PSD. Overall, the correspondence is a good indication that both models are able to model the initialization phase acceptably well. Moreover, the time scales in concentration are quantitatively comparable for the results of both models. We conclude that both models can be used interchangeably for our application, leaving the choice to the user based on specific needs and considerations. We will elaborate upon these considerations in the next section.

The analysis presented in this research provides a general framework to investigate the effects of spine morphology on the surface diffusion of receptors within the cell membrane. In the case of spiny dendrites, it allows us to take into account multiple spines with various shapes. This is important from a biological modeling perspective, since both the location of spines as well as their shape are diverse.

7.2. DISCUSSION AND RECOMMENDATIONS

7.2.1. CHOSEN MORPHOLOGY FOR DENDRITIC SPINES

In this section we will zoom in on assumptions we made and present their implications. Some of these implications result in recommendations for future research and we will also present them here.

Capturing the typical features of spine morphology could be improved upon. The geometries we choose have the drawback that the thin and filopodia spines cannot be well represented, as can been seen from Figure 4.3. The cause is that these shapes are not able to display the characteristic neck specific to thin and filopodia spines. It would be interesting to consider shapes that do incorporate these distinctive long necks, so that also the influence of neck length and width on interspinal crosstalk can be investigated. Miermans et al. developed a model that incorporates this feature concurrently with the development of this work [51]. Since the models we propose put little restrictions on the spinal shapes, these results can be used for future research.

A more ad hoc method to incorporate the spine neck is to take a closer look at the shapes we already use. During the formation of these shapes there is a moment in which a neck, although it is a short one, is formed. The stages before this point can be used as a model for stubby spines, stages after can be used as a model for mushroom-shaped spines and this point itself can be used as a model for filopodia-shaped spines. These three stages are shown in Figure 7.1.

At the moment a neck is formed, these shapes have a vertical part ($\frac{\mathrm{d}s}{\mathrm{d}x} = 0$ in 2D, $\frac{\mathrm{d}s}{\mathrm{d}x} = \frac{\mathrm{d}s}{\mathrm{d}y} = 0$ in 3D). This neck can be extended to form the typical long neck, characteristic to thin and filopodia shaped spines. This is illustrated in Figure 7.2.

Another extension is to change the orientation of the spine relative to the dendritic surface. Currently, the longitudinal axis of the spine is perpendicular to the dendritic surface. However, in reality this is not always the case. A model with the possibility to change the angle between the longitudinal axis of the spine and the dendritic surface could help in assessing what the influence is of this angle on the diffusion process and corresponding characteristics like time to equilibrium and (conditional) mean first passage times.

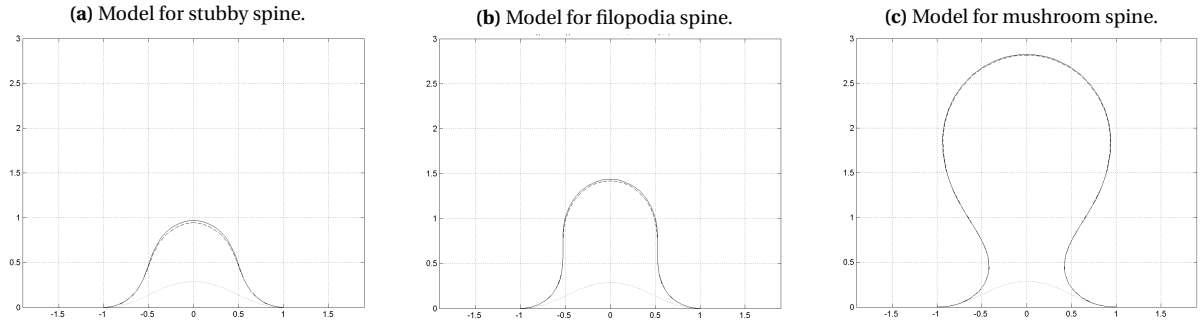

(a) Model for stubby spine. **(b)** Model for filopodia spine. **(c)** Model for mushroom spine.

Figure 7.1: Intersection of three shapes. (a) Shape before neck formation. (b) Shape at neck formation. (c) Shape after neck formation. Results produced by [42].

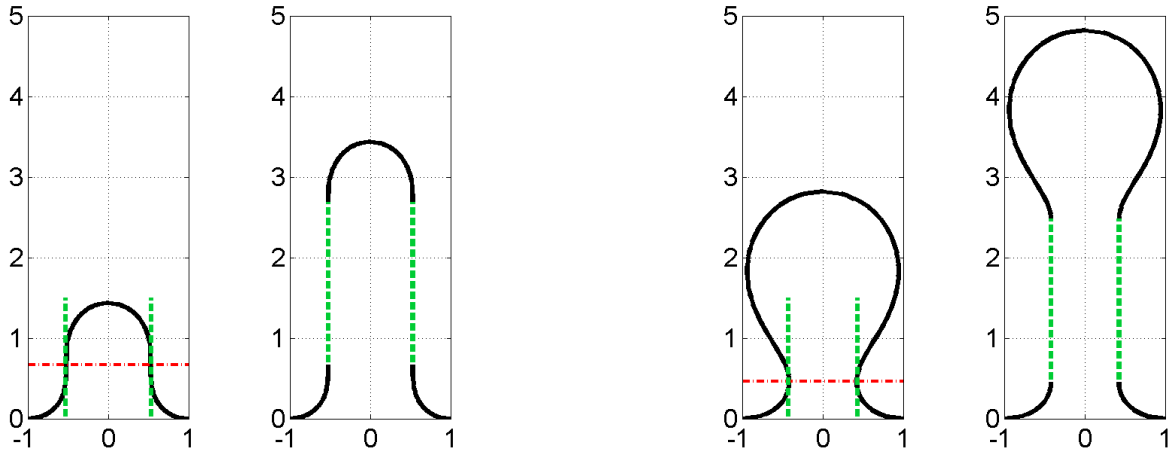

(a) Filopodia spine. **(b)** Mushroom spine.

Figure 7.2: Suggestion of procedure to create characteristic spine neck. This procedure could be used to also extend models for filopodia and thin spines.

7.2.2. COMPARISON OF BOTH MODELS

In Section 4.4 we discussed the design differences between our particle-based and concentration-based model. Here we give a brief recapitulation and add the difference in performance between the models. The advantages and disadvantages of both models can be found in Table 7.1. Many of them are discussed earlier and we elaborate upon the enumerated ones here.

1. Single particle tracking (SPT) is an experimental technique in which motion of individual particles in a medium is observed [30]. Since the particle-based model simulates trajectories of individual particles, the results of this model are highly suitable to be compared to SPT data.

2. When simulating diffusion in a Euclidean space like $\mathbb{R}^2$ or $\mathbb{R}^3$, the choice of the step size λ does not cause problems in general, as long as it is chosen in proportion to the time step as suggested in Algorithm 2. This is due to the fact that spatial steps within one iteration are (straight) lines. In our case, however, we want to move a distance λ along a geodesic curve on a two dimensional manifold, which is not generally straight. This is performed by taking a second order approximation of the surface. This induces a length scale at every point of this surface in which this approximation is valid. If λ exceeds this scale our method becomes insensitive to features of the manifold which are smaller than this scale. This imposes a restriction in our choice of λ and therefore in our choice of time step. Making λ location dependent could be beneficial for places where the two dimensional manifold resembles a plane, but

	Model I	
+	Extraction of statistics such as mean first passage time and crosstalk.	
+	Flexibility in domain composition, implementation of boundary conditions, and initation of trajectories.	
+	Similarity to experimental techniques such as single particle tracking (SPT).	1
-	Presence of stochastic fluctuations when interested in concentration profiles.	
-	Computational intensity rises with number of particles.	
-	Restriction size of time step due to curvature of the surface.	2
	Model II	
+	Suitable when interested in concentration profiles.	
+	Choice of time step only depending on numerical method, not on curvature of surface.	3
+	Similarity to experimental techniques such as fluorescence recovery after photobleaching (FRAP).	4
-	Extraction of statistics such as mean first passage time means solving another system, hence dramatically increasing computation time.	5
-	Less flexibility in domain composition, exotic boundary conditions and introducing single particles.	

Table 7.1: Advantages and disadvantages of both models. All numbered considerations are elaborated upon in this section.

this is implementational cumbersome, because elapsed time would have to be tracked for individual particles.

3. In the case of the concentration-based model, we do not have such restrictions on the time step. A sharper curvature is dealt with by refining the grid at such places. Of course, refining a grid implies having more basis functions and therefore the system that has to be solved every iteration will increase in dimension. This is at the expense of computational time per iteration, but does not immediately impose a restriction on the step size.

   Using an implicit time integration method does not restrict the time step in order to get stability. However, the time step should be proportional to the size of our elements in order to get acceptable accuracy. Still, the time step used in the concentration-based model ($\Delta t = 0.5s$) is significantly larger than the chosen time step in the particle-based model ($\Delta t = 0.00025s$).

4. Fluorescence recovery after photobleaching (FRAP) is an experimental technique capable of quantifying lateral diffusion in a thin film [29]. Part of this film is photobleached by a light pulse, after which the intensity is monitored as the bleached part diffuses out and unbleached part diffuses in. By introducing a new variable of concentration of photobleached particles C_{FRAP}, the results of the concentration-based model are highly suitable to be compared to FRAP data.

5. Statistics such as the mean first passage time or the level of crosstalk cannot easily be obtained from the results of model II. Although the mean first passage time can generally be obtained by solving a relative time independent system [36], for our definition of crosstalk no analog exist in the framework of partial differential equations. Additionally, defining and calculating standard deviations is complicated. It is unclear of such an analog can be derived, but if possible, the solution would have to be sought in the application stochastic differential calculus. As for now, this model is unsuitable to calculate such statistics.

The choice between these two models will have to be made based on specific needs. When interested in concentration primarily, the concentration-based model should be preferred, because the particle-based model will have to simulate many particles to damp stochastic fluctuations, increasing computation time and memory usage. The computation time for the particle-based model with 10^4 particles, with $T_{end} = 300s$ is approximately 25 hours. The computation time for the concentration-based model with ≈ 250 elements (after refining grid) is approximately 2 hours. When the objective is to assess the level of crosstalk or other statistics, the particle-based model is a better suited model, which also provides a lot of flexibility.

7.2.3. COMPARISON TO EXPERIMENTAL DATA

An open question is still to what extent our models correspond to experimental data. Especially SPT is a good candidate to analyze whether the discussed models are a suitable way to address interspinal crosstalk. The techniques we propose integrate lateral diffusion on curved surfaces and anchoring at the PSD, but in the case of receptor diffusion on a cell membrane, more processes are involved. The Cell Biology research division of the Biology Department of the Faculty of Science at Utrecht University is making great progress in making such analysis possible and data should be available soon.

A

ILLUSTRATING MOVIES

Here we give a short description of the short movies we present. The movies can be downloaded from github.com/TamaraKloek/spineMorphology.

Movie A1. Simulation of particle-based model. Dendritic exocytosis, trapping at PSD is incorporated.

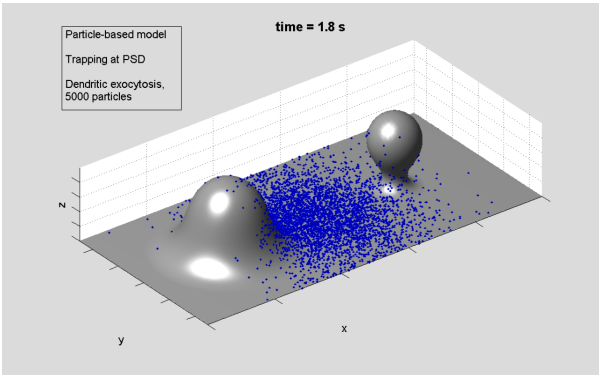

Movie A2a. Simultion of particle-based model. Spinal exocytosis in a spine with shape parameter $A = 1.5$, trapping at PSD is incorporated.

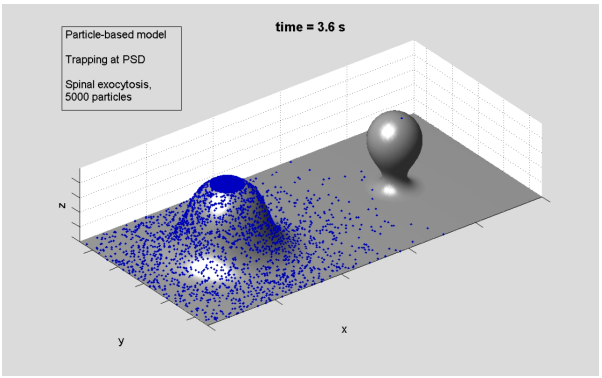

Movie A2b. Simultion of particle-based model. Spinal exocytosis in a spine with shape parameter $A = 5.0$, trapping at PSD is incorporated.

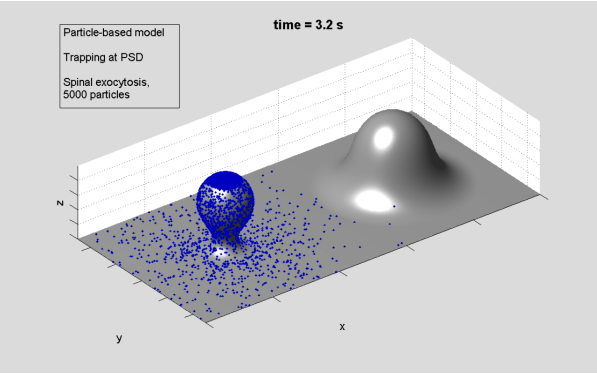

Movie A3. Simultion of concentration-based model. Dendritic exocytosis, trapping at PSD is incorporated.

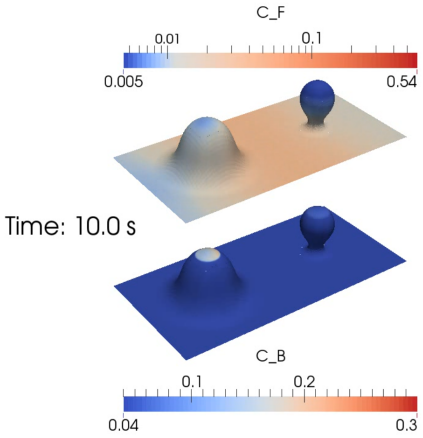

B

PARAMETRIZATION OF THE SURFACE Ω

For the domain Ω we have a global parametrization, $\mathcal{S}(\alpha,\beta)$, with $(\alpha,\beta)\in\Omega_0$. When located on the dendrite, i.e. $r(\alpha,\beta)\in\Omega_{dendrite}$, we have,

$$\mathcal{S}(\alpha,\beta)=\begin{pmatrix}\alpha\\ \beta\\ 0\end{pmatrix},\quad (\alpha,\beta)\in\Omega_{dendrite}. \tag{B.1}$$

The surfaces of the dendritic spines, Ω_j, are modeled as axisymmetric. It is a surface of revolution around a vector in the direction of the z-axis. Let $(\hat{\alpha},\hat{\beta})$ be the coordinate on the surface Ω_0 where this vector intersects Ω_0. The generatix of the surface of revolution is a curve in the r,z-plane, parameterized by u. This gives the spine its own local parameterization,

$$\begin{aligned}&\vec{r}\,(u,\theta)=\begin{pmatrix}\hat{\alpha}\\ \hat{\beta}\\ 0\end{pmatrix}+\begin{pmatrix}r(u)\cos(\theta)\\ r(u)\sin(\theta)\\ z(u)\end{pmatrix},\\ &\text{where } r(u) \text{ and } z(u) \text{ given functions and } (\theta,u)\in([0,2\pi],[0,u_{max}])\,,\end{aligned} \tag{B.2}$$

with the following associated metric:

$$g_{u\theta}:=\begin{pmatrix}\boldsymbol{r}_u\cdot\boldsymbol{r}_u & \boldsymbol{r}_u\cdot\boldsymbol{r}_\theta\\ \boldsymbol{r}_\theta\cdot\boldsymbol{r}_u & \boldsymbol{r}_u\cdot\boldsymbol{r}_u\end{pmatrix}=\begin{pmatrix}z'(u)^2+r'(u)^2 & 0\\ 0 & r(u)^2\end{pmatrix}.$$

From this we can derive the following non-zero Christoffel symbols:

$$\begin{aligned}\Gamma^u_{uu} &= \tfrac{r'(u)r''(u)+z'(u)z''(u)}{r'(u)^2+z'(u)^2},\\ \Gamma^u_{\theta\theta} &= -\tfrac{r(u)r'(u)}{r'(u)^2+z'(u)^2},\\ \Gamma^\theta_{u\theta} &= \tfrac{r(u)r'(u)}{r(u)^2}.\end{aligned}$$

We consider diffusion on this surface of revolution, with constant diffusion coefficient D, which can be described by the following differential equation:

$$\frac{\partial c}{\partial t}=D\nabla_g^2 c,$$

where $c(z,t)$ denotes the concentration of certain particles and where ∇_g^2 denotes the Laplace-Beltrami operator. The Laplace-Beltrami operator can be calculated from the metric and Christoffel symbols,

$$\begin{aligned}\nabla_g^2 &= g^{jk}\frac{\partial^2}{\partial x^k \partial x^j} - g^{jk}\Gamma^l_{kj}\frac{\partial}{\partial x^l} \\ &= g^{uu}\frac{\partial^2}{\partial u^2} - g^{uu}\Gamma^u_{uu}\frac{\partial}{\partial u} + g^{\theta\theta}\frac{\partial^2}{\partial \theta^2} - g^{\theta\theta}\Gamma^u_{\theta\theta}\frac{\partial}{\partial u},\end{aligned}$$

where g_{ij} are entries of the of the metric and g^{ij} entries of the matrix inverse to the metric.

The last needed ingredient is a transformation from the global coordinates on the base of the dendrite $(\alpha,\beta) \in \Omega_j^{base}$, to the local coordinates (u,θ). This transformation is defined as

$$\begin{aligned}u &= \frac{\sqrt{(\alpha-\hat{\alpha})^2+(\beta-\hat{\beta})^2}}{R_j^{exit}}u_{max}, \\ \theta &= \arctan\left(\frac{\beta-\hat{\beta}}{\alpha-\hat{\alpha}}\right).\end{aligned}$$

The complete global parametrization of the surface Ω is then as Eq. (B.1) for $(\alpha,\beta) \in \Omega_{dendrite}$ and as (B.2) for $|(\alpha,\beta) - \boldsymbol{r}_j| < R_j^{exit}$.

C

DETAILS ON THE FEM SCHEME

The implementation and execution of the FEM-scheme is handled by Nutils, an open source Python programming library for finite element applications. More information on Nutils can be found on nutils.org. The software package can be downloaded on GitHub: github.com/nutils.

Nutils requires a weak form to be provided by the user and we present details on the derivation of that weak form. Furthermore, we elaborate upon some implementational details regarding exocytosis and PSD.

C.1. WEAK FORMULATION

The system of partial differential equations we consider is given in Eq. (4.4):

$$\begin{cases} \dfrac{\partial C_F}{\partial t} &= D\nabla_g^2 C_F &- K_{on}C_F + K_{off}C_B, \\ \dfrac{\partial C_B}{\partial t} &= &K_{on}C_F - K_{off}C_B, \end{cases}$$

where K_{on} and K_{off} are defined as in Eq. (4.5) and ∇_g^2 denotes the Laplace-Beltrami operator associated with the metric g as defined in Section 4.1.2 and Appendix B. Initial conditions are as in Eq. (4.6):

$$\begin{aligned} C_F(\boldsymbol{r},0) &= \begin{cases} c_0 & \boldsymbol{r} \in A_{exo}, \\ 0 & \text{otherwise}, \end{cases} \\ C_B(\boldsymbol{r},0) &= 0 \qquad \text{everywhere}. \end{aligned}$$

We call the boundary Γ and boundary conditions are as in Eqs. (4.7), (4.8):

$$\begin{aligned} C(x,y,t) &= C(x,y+2\pi R_d,t), \qquad \forall\, y, \\ \frac{\partial C}{\partial x}(0,y,t) &= \frac{\partial C}{\partial x}(l,y,t) = 0. \end{aligned}$$

We derive the weak formulation for the first equation of (4.4), the derivation for the second is similar. Multiply the equation with a test function $\varphi \in H^1(\Omega) = \{f \in L^2(\Omega) \mid f \text{ has a weak derivative}\}$ (first Sobolev space), that satisfies the boundary conditions (4.7, 4.8), and integrate over our curved domain Ω:

$$\int_\Omega \frac{\partial C_F}{\partial t}\varphi \,\mathrm{d}\Omega = D\int_\Omega \nabla_g^2 C_F\varphi \,\mathrm{d}\Omega - \int_\Omega K_{on}C_F\varphi \,\mathrm{d}\Omega + \int_\Omega K_{off}C_B\varphi \,\mathrm{d}\Omega.$$

By partial differentiation and Gauss's theorem (divergence theorem), we have

$$\begin{aligned}\int_\Omega \frac{\partial C_F}{\partial t}\varphi \,\mathrm{d}\Omega &= D\int_\Omega \nabla_g\left[\varphi\nabla_g C\right]\mathrm{d}\Omega - D\int_\Omega \langle\nabla_g\varphi,\nabla_g C\rangle_g \,\mathrm{d}\Omega - \int_\Omega K_{on}C_F\varphi \,\mathrm{d}\Omega + \int_\Omega K_{off}C_B\varphi \,\mathrm{d}\Omega\\ &= D\int_\Gamma \langle\varphi\nabla_g C,\hat{n}\rangle_g \,\mathrm{d}\Gamma - D\int_\Omega \langle\nabla_g\varphi,\nabla_g C\rangle_g \,\mathrm{d}\Omega - \int_\Omega K_{on}C_F\varphi \,\mathrm{d}\Omega + \int_\Omega K_{off}C_B\varphi \,\mathrm{d}\Omega\\ &= D\int_\Gamma \varphi\frac{\partial C}{\partial\hat{n}}\,\mathrm{d}\Gamma - D\int_\Omega \langle\nabla_g\varphi,\nabla_g C\rangle_g \,\mathrm{d}\Omega - \int_\Omega K_{on}C_F\varphi \,\mathrm{d}\Omega + \int_\Omega K_{off}C_B\varphi \,\mathrm{d}\Omega,\end{aligned}$$

where $\hat{n}$ denotes the vector normal to Γ of unit length.

Let us have a closer look at the integral in the first term, $\int_\Gamma \varphi\frac{\partial C}{\partial\hat{n}}\,\mathrm{d}\Gamma$. Γ is the boundary of our domain shown in Figure 4.1. This boundary consists of the boundaries at $x=0, x=l, y=-\pi R_d$ and $y=\pi R_d$, which we call the east, west, south and north boundary respectively. We get

$$\begin{aligned}\int_\Gamma \varphi\frac{\partial C}{\partial\hat{n}}\,\mathrm{d}\Gamma &= \int_{\Gamma_{north}} \varphi\frac{\partial C}{\partial\hat{n}}\,\mathrm{d}\Gamma + \int_{\Gamma_{east}} \varphi\frac{\partial C}{\partial\hat{n}}\,\mathrm{d}\Gamma + \int_{\Gamma_{south}} \varphi\frac{\partial C}{\partial\hat{n}}\,\mathrm{d}\Gamma + \int_{\Gamma_{west}} \varphi\frac{\partial C}{\partial\hat{n}}\,\mathrm{d}\Gamma\\ &= \int_{\Gamma_{north}} \varphi\frac{\partial C}{\partial y}\,\mathrm{d}\Gamma + \int_{\Gamma_{east}} \varphi\frac{\partial C}{\partial x}\,\mathrm{d}\Gamma - \int_{\Gamma_{south}} \varphi\frac{\partial C}{\partial y}\,\mathrm{d}\Gamma - \int_{\Gamma_{west}} \varphi\frac{\partial C}{\partial x}\,\mathrm{d}\Gamma.\end{aligned} \tag{C.1}$$

By the boundary condition of Equation (4.8), the integrals for the left and right boundary vanish. By the boundary condition of Eq. (4.7) we have

$$\varphi\frac{\partial C}{\partial y}\bigg|_{\Gamma_{north}} = \varphi\frac{\partial C}{\partial y}\bigg|_{\Gamma_{south}}.$$

Therefore, all terms of Eq. (C.1) either vanish or cancel each other out and we find

$$\int_\Gamma \varphi\frac{\partial C}{\partial\hat{n}}\,\mathrm{d}\Gamma = 0,$$

leading to the weak form,

$$\int_\Omega \frac{\partial C_F}{\partial t}\varphi \,\mathrm{d}\Omega = -D\int_\Omega \langle\nabla_g\varphi,\nabla_g C\rangle_g \,\mathrm{d}\Omega - \int_\Omega K_{on}C_F\varphi \,\mathrm{d}\Omega + \int_\Omega K_{off}C_B\varphi \,\mathrm{d}\Omega. \tag{C.2}$$

C.2. DISCRETIZATION

The concentration of free particles is approximated by $C_F \approx \widetilde{C}_F = \sum_{j=1}^N \widetilde{C}_F^j(t)\varphi_j(\boldsymbol{r})$ and the concentration of bound particles by $C_B \approx \widetilde{C}_B = \sum_j \widetilde{C}_B^j(t)\varphi_j(\boldsymbol{r})$. Here, the collection $\{\varphi_1,\ldots,\varphi_N\}$, is a set of linearly independent basis functions. We use B-splines of degree p. These splines are extensively discussed in [52]. Furthermore, we introduce a discretization in time and use the following approximation for $\frac{\partial C_F}{\partial t}$ at time $t = m\Delta t$,

$$\frac{\partial C_F}{\partial t} \approx \frac{\partial\widetilde{C}_F}{\partial t}\bigg|_m \approx \frac{\widetilde{C}_F|_{m+1} - \widetilde{C}_F|_m}{\Delta t}.$$

In Eq. (C.2) we set $\varphi \equiv \varphi_i$. This results in the following implicit relation,

$$\begin{aligned}\int_\Omega \frac{\widetilde{C}_F\big|_{m+1} - \widetilde{C}_F\big|_m}{\Delta t}\varphi_i \,\mathrm{d}\Omega = &-D\sum_j \widetilde{C}_F^j\Big|_{m+1} \cdot \int_\Omega \langle \nabla_g \varphi_i, \nabla_g \varphi_j \rangle_g \,\mathrm{d}\Omega \\ &+ \sum_j \widetilde{C}_B^j\Big|_{m+1} \cdot \int_\Omega K_{off}\varphi_i\varphi_j \,\mathrm{d}\Omega \\ &- \sum_j \widetilde{C}_F^j\Big|_{m+1} \cdot \int_\Omega K_{on}\varphi_i\varphi_j \,\mathrm{d}\Omega.\end{aligned}$$

Which leads to

$$\begin{aligned}\frac{\sum_j \left(\widetilde{C}_F^j\Big|_{m+1} - \widetilde{C}_F^j\Big|_m\right)}{\Delta t}\int_\Omega \varphi_i\varphi_j \,\mathrm{d}\Omega = &-D\sum_j \widetilde{C}_F^j\Big|_{m+1} \cdot \int_\Omega \langle \nabla_g \varphi_i, \nabla_g \varphi_j \rangle_g \,\mathrm{d}\Omega \\ &+ \sum_j \widetilde{C}_B^j\Big|_{m+1} \cdot \int_\Omega K_{off}\varphi_i\varphi_j \,\mathrm{d}\Omega \\ &- \sum_j \widetilde{C}_F^j\Big|_{m+1} \cdot \int_\Omega K_{on}\varphi_i\varphi_j \,\mathrm{d}\Omega.\end{aligned} \tag{C.3}$$

We define the following notation.

- Let $[\widetilde{C}_F]$ denote the vector containing the coefficients $\widetilde{C}_F^j$;
- Let M the mass-matrix of which the entries m_{ij} are defined by $\int_\Omega \varphi_i\varphi_j \,\mathrm{d}\Omega$;
- Let $\mathcal{K}_{on}$ the matrix of which the entries are defined by $\int_\Omega K_{on}\varphi_i\varphi_j \,\mathrm{d}\Omega$;
- Let $\mathcal{K}_{off}$ the matrix of which the entries are defined by $\int_\Omega K_{off}\varphi_i\varphi_j \,\mathrm{d}\Omega$;
- Let L be the matrix of which the entries are defined by $\int_\Omega \langle \nabla_g \varphi_i, \nabla_g \varphi_j \rangle_g \,\mathrm{d}\Omega$.

Then we can reformulate Eq. (C.3) as

$$M\frac{[\widetilde{C}_F]_{m+1} - [\widetilde{C}_F]_m}{\Delta t} = -DL[\widetilde{C}_F]_{m+1} + \mathcal{K}_{off}[\widetilde{C}_B]_{m+1} - \mathcal{K}_{on}[\widetilde{C}_F]_{m+1}.$$

Rearranging terms leads to

$$\left(M + \Delta t\cdot(DL + \mathcal{K}_{on})\right)[\widetilde{C}_F]_{m+1} - \Delta t\cdot\mathcal{K}_{off}[\widetilde{C}_B]_{m+1} = M[\widetilde{C}_F]_m. \tag{C.4}$$

Similarly, we find the discrete counterpart of the second equation of (4.4),

$$\left(M + \Delta t\cdot\mathcal{K}_{off}\right)[\widetilde{C}_B]_{m+1} - \Delta t\cdot\mathcal{K}_{on}[\widetilde{C}_F]_{m+1} = M[\widetilde{C}_B]_m. \tag{C.5}$$

If we combine Eq. (C.4) and Eq. (C.5), we obtain the following linear system,

$$\begin{bmatrix} M + \Delta t\cdot(DL + \mathcal{K}_{on}) & -\Delta t\cdot\mathcal{K}_{off} \\ -\Delta t\cdot\mathcal{K}_{on} & M + \Delta t\cdot\mathcal{K}_{off} \end{bmatrix}\begin{bmatrix} \widetilde{C}_F \\ \widetilde{C}_B \end{bmatrix}_{m+1} = \begin{bmatrix} M & \varnothing \\ \varnothing & M \end{bmatrix}\begin{bmatrix} \widetilde{C}_F \\ \widetilde{C}_B \end{bmatrix}_m.$$

C.3. IMPLEMENTATION OF EXOCYTOSIS AND PSD

The functions K_{on} and K_{off} as in Equation (4.5) and the function $C_F(\boldsymbol{r},0)$ as in Equation (4.6) are discontinuous functions defined on the the domain of computation. Because projection of discontinuous functions on the space spanned by the basis functions $\{\varphi_1,\ldots,\varphi_N\}$ might lead to oscillations, we choose to approximate the discontinuities of these functions using the sigmoid function hyperbolic tangent (tanh). This way, we create a smooth version of these functions, eliminating discontinuities.

The initial condition is implemented by projecting the smooth version of $C_F(\boldsymbol{r},0)$ onto the space spanned by the basis vectors φ_i.

D

DETAILS ON IMPLEMENTATION OF PARTICLE-BASED MODEL

Here we discuss some details concerning the implementation of the particle-based model. Because our domain is a composition of dendrite and spines, in the implementation of this model we use a domain decomposition for the different components. First we briefly discuss how this is handled. Second, we give a schematic representation of our algorithm.

D.1. DOMAIN DECOMPOSITION

Our domain Ω is a composition of the dendrite, $\Omega_{dendrite}$, the spines Ω_j and the boundaries between these two $\partial\Omega_j$, as defined in Equation 4.1.1. These domains have their own local parametrization and metric, as defined in Appendix B. We apply a domain decomposition in which we decompose the domain Ω again in the dendrite and individual spines.

Every iteration we determine which particles are in what domain and then we apply the diffusion per domain separately. This way we get around transforming every iteration from global to local parametrizations and vice versa, which saves arithmetic operations. Particles are set to diffuse inside a domain until it reaches a boundary between domains. For simplicity, when a boundary is reached, we place the particle on the boundary and set it to diffuse in the other domain than where it came from. For example, when a particle diffuses over the dendrite ($\Omega_{dendrite}$) and reaches the boundary $\partial\Omega_j$ with spine j (Ω_j), it is set on the boundary $\partial\Omega_j$ and next iteration will diffuse over Ω_j.

D.2. SCHEMATIC REPRESENTATION OF THE ALGORITHM

In Figure D.1 the algorithm used for the particle-based model is schematically shown. Input are the parameters as defined in Table 4.1 and the surface, which is parametrized as explained in Appendix B. The implementation of this model was done in Matlab.

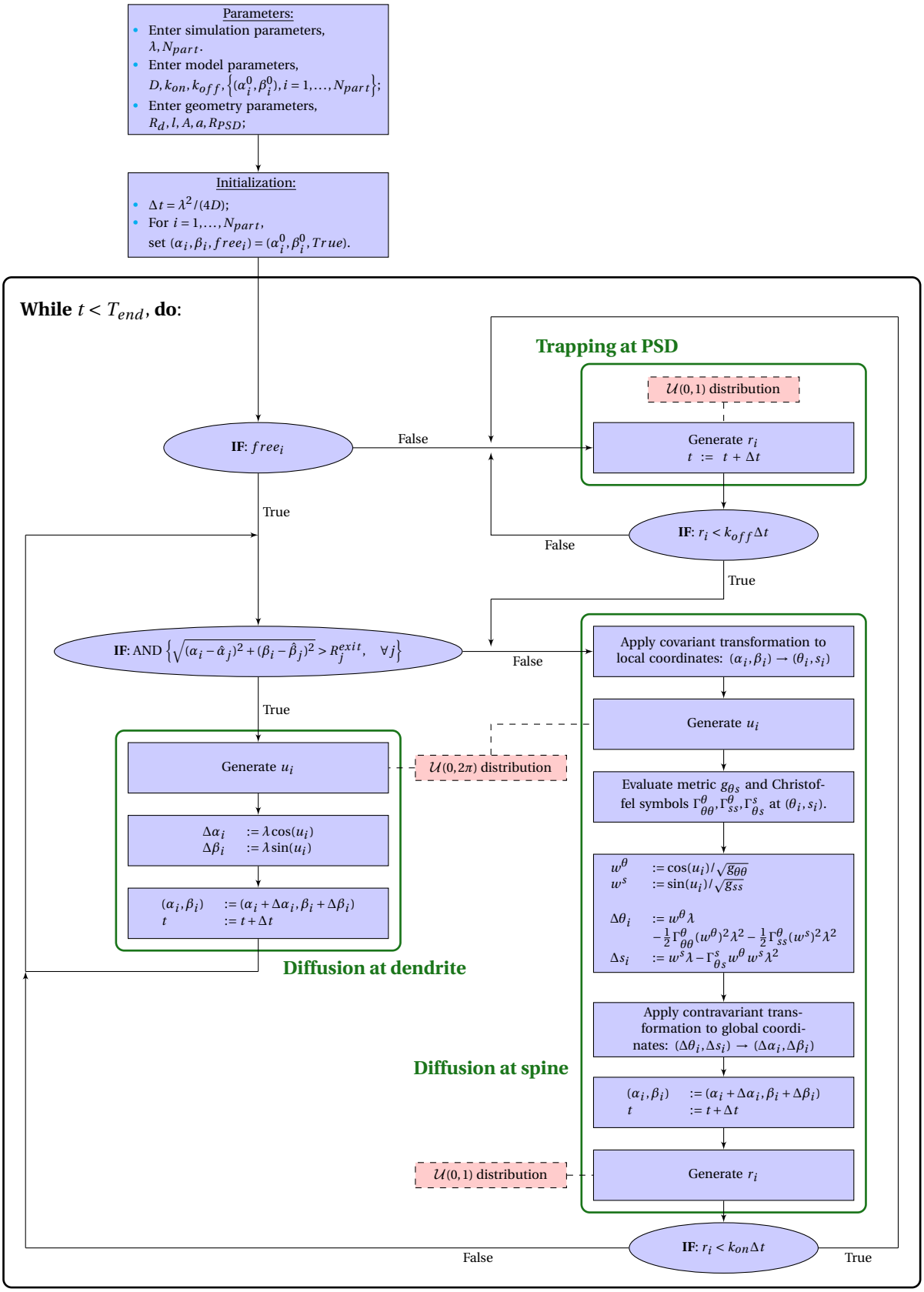

Figure D.1: Flow chart depicting algorithm used in model I.

BIBLIOGRAPHY

[1] R. Kusters, L. C. Kapitein, C. C. Hoogenraad, and C. Storm, *Shape-induced asymmetric diffusion in dendritic spines allows efficient synaptic AMPA receptor trapping,* Biophysical Journal **105**, 2743 (2013).

[2] R. Kusters and C. Storm, *Impact of morphology on diffusive dynamics on curved surfaces,* Physical Review E **89** (2014), 10.1103/PhysRevE.89.032723.

[3] D. C. Javitt, *Glutamate as a therapeutic target in psychiatric disorders,* Molecular Psychiatry **9**, 984 (2004).

[4] G. Dawson, *Early behavioral intervention, brain plasticity, and the prevention of autism spectrum disorder,* Development and Psychopathology **20**, 775 (2008).

[5] V. A. Derkach, M. C. Oh, E. S. Guire, and T. R. Soderling, *Regulatory mechanisms of AMPA receptors in synaptic plasticity,* Nature Reviews Neuroscience **8**, 101 (2007).

[6] T. C. Sudhof, *The synaptic vesicle cycle,* Annual Review of Neuroscience **27**, 509 (2004).

[7] M. Sheng and C. C. Hoogenraad, *The postsynaptic architecture of excitatory synapses: a more quantitative view,* Annual Review of Biochemistry **76**, 823 (2007).

[8] S. Naisbitt, E. Kim, J. C. Tu, B. Xiao, C. Sala, J. Valtschanoff, R. J. Weinberg, P. F. Worley, and M. Sheng, *Shank, a novel family of postsynaptic density proteins that binds to the NMDA receptor/PSD-95/GKAP complex and cortactin,* Neuron **23**, 569 (1999).

[9] M. Hollmann and S. Heinemann, *Cloned glutamate receptors,* Annual review of neuroscience **17**, 31 (1994).

[10] R. M. Julien, *A primer of drug action: A concise, nontechnical guide to the actions, uses, and side effects of psychoactive drugs* (WH Freeman, Times Books, Henry Holt & Co, 1995).

[11] H. Kasai, M. Matsuzaki, J. Noguchi, N. Yasumatsu, and H. Nakahara, *Structure–stability–function relationships of dendritic spines,* Trends in Neurosciences **26**, 360 (2003).

[12] J. I. Arellano, R. Benavides-Piccione, J. DeFelipe, and R. Yuste, *Ultrastructure of dendritic spines: correlation between synaptic and spine morphologies,* Frontiers in Neuroscience **1**, 131 (2007).

[13] T. Tada and M. Sheng, *Molecular mechanisms of dendritic spine morphogenesis,* Current Opinion in Neurobiology **16**, 95 (2006).

[14] I. M. Ethell and E. B. Pasquale, *Molecular mechanisms of dendritic spine development and remodeling,* Progress in Neurobiology **75**, 161 (2005).

[15] R. Yuste and T. Bonhoeffer, *Morphological changes in dendritic spines associated with long-term synaptic plasticity,* Annual review of neuroscience **24**, 1071 (2001).

[16] J. Tønnesen, G. Katona, B. Rózsa, and U. V. Nägerl, *Spine neck plasticity regulates compartmentalization of synapses,* Nature neuroscience **17**, 678 (2014).

[17] M. Adrian, R. Kusters, C. J. Wierenga, C. Storm, C. C. Hoogenraad, and L. C. Kapitein, *Barriers in the brain: resolving dendritic spine morphology and compartmentalization,* Frontiers in Neuroanatomy **8**, 142 (2014).

[18] S. Martin, P. Grimwood, and R. Morris, *Synaptic plasticity and memory: an evaluation of the hypothesis,* Annual review of neuroscience **23**, 649 (2000).

[19] B. B. Johansson, *Brain plasticity and stroke rehabilitation: The Willis lecture,* Stroke **31**, 223 (2000).

[20] K. Gerrow and A. Triller, *Synaptic stability and plasticity in a floating world,* Current Opinion in Neurobiology **20**, 631 (2010).

[21] J.-L. Gaiarsa, O. Caillard, and Y. Ben-Ari, *Long-term plasticity at gabaergic and glycinergic synapses: mechanisms and functional significance,* Trends in Neurosciences **25**, 564 (2002).

[22] T. V. Bliss and G. L. Collingridge, *A synaptic model of memory: long-term potentiation in the hippocampus,* Nature **361**, 31 (1993).

[23] A. Peters and I. R. Kaiserman-Abramof, *The small pyramidal neuron of the rat cerebral cortex. the perikaryon, dendrites and spines.* American Journal of Anatomy **127**, 321 (1970).

[24] C. Cheng, O. Trzcinski, and L. C. Doering, *Fluorescent labeling of dendritic spines in cell cultures with the carbocyanine dye "Dil",* Frontiers in neuroanatomy **8** (2014).

[25] K. Czöndör, M. Mondin, M. Garcia, M. Heine, R. Frischknecht, D. Choquet, J.-B. Sibarita, and O. R. Thoumine, *Unified quantitative model of AMPA receptor trafficking at synapses,* Proceedings of the National Academy of Sciences **109**, 3522 (2012).

[26] H.-C. Kornau, L. T. Schenker, M. B. Kennedy, and P. H. Seeburg, *Domain interaction between NMDA receptor subunits and the postsynaptic density protein PSD-95,* Science **269**, 1737 (1995).

[27] A. Triller and D. Choquet, *New concepts in synaptic biology derived from single-molecule imaging,* Neuron **59**, 359 (2008).

[28] D. Meyer, T. Bonhoeffer, and V. Scheuss, *Balance and stability of synaptic structures during synaptic plasticity,* Neuron **82**, 430 (2014).

[29] D. Axelrod, D. Koppel, J. Schlessinger, E. Elson, and W. Webb, *Mobility measurement by analysis of fluorescence photobleaching recovery kinetics,* Biophysical journal **16**, 1055 (1976).

[30] M. J. Saxton and K. Jacobson, *Single-particle tracking: applications to membrane dynamics,* Annual review of biophysics and biomolecular structure **26**, 373 (1997).

[31] D. M. Kullmann, G. Erdemli, and F. Asztély, *Ltp of ampa and nmda receptor–mediated signals: evidence for presynaptic expression and extrasynaptic glutamate spill-over,* Neuron **17**, 461 (1996).

[32] D. M. Kullmann and F. Asztely, *Extrasynaptic glutamate spillover in the hippocampus: evidence and implications,* Trends in neurosciences **21**, 8 (1998).

[33] D. Holcman and Z. Schuss, *Diffusion laws in dendritic spines,* The Journal of Mathematical Neuroscience **1**, 10 (2011).

[34] Z. Schuss, *Theory and applications of stochastic processes: an analytical approach*, Vol. 170 (Springer Science & Business Media, 2009).

[35] M. Christensen, *How to simulate anisotropic diffusion processes on curved surfaces,* Journal of Computational Physics **201**, 421 (2004).

[36] N. Ikeda and S. Watanabe, *Stochastic differential equations and diffusion processes* (North-Holland/Kodansha, 1989).

[37] P. C. Bressloff, B. A. Earnshaw, and M. J. Ward, *Diffusion of protein receptors on a cylindrical dendritic membrane with partially absorbing traps,* SIAM Journal on Applied Mathematics **68**, 1223 (2008).

[38] B. A. Earnshaw and P. C. Bressloff, *Biophysical model of AMPA receptor trafficking and its regulation during long-term potentiation/long-term depression,* Journal of Neuroscience **26**, 12362 (2006).

[39] D. Holcman and A. Triller, *Modeling synaptic dynamics driven by receptor lateral diffusion,* Biophysical Journal **91**, 2405 (2006).

[40] B. A. Earnshaw and P. C. Bressloff, *Modeling the role of lateral membrane diffusion in AMPA receptor trafficking along a spiny dendrite,* Journal of Computational Neuroscience **25**, 366 (2008).

[41] F. Debbasch and C. Chevalier, *Diffusion processes on manifolds,* in *Markov Processes and Related Topics: A Festschrift for Thomas G. Kurtz*, Collections, Vol. 4, edited by S. N. Ethier, J. Feng, and R. H. Stockbridge (Institute of Mathematical Statistics, Beachwood, Ohio, USA, 2008) pp. 85–97.

[42] K. Miermans, R. Kusters, and C. Storm, *On the morphology of dendritic spines,* (2015), part of master thesis at TU Eindhoven.

[43] P. B. Canham, *The minimum energy of bending as a possible explanation of the biconcave shape of the human red blood cell,* Journal of Theoretical Biology **26**, 61 (1970).

[44] W. Helfrich, *Elastic properties of lipid bilayers: theory and possible experiments,* Zeitschrift für Naturforschung C **28**, 693 (1973).

[45] D. S. Bredt and R. A. Nicoll, *AMPA receptor trafficking at excitatory synapses,* Neuron **40**, 361 (2003).

[46] M. A. Patterson, E. M. Szatmari, and R. Yasuda, *AMPA receptors are exocytosed in stimulated spines and adjacent dendrites in a Ras-ERK–dependent manner during long-term potentiation,* Proceedings of the National Academy of Sciences **107**, 15951 (2010).

[47] I. Nikonenko, B. Boda, S. Steen, G. Knott, E. Welker, and D. Muller, *PSD-95 promotes synaptogenesis and multiinnervated spine formation through nitric oxide signaling,* The Journal of cell biology **183**, 1115 (2008).

[48] J. R. Cottrell, G. R. Dubé, C. Egles, and G. Liu, *Distribution, density, and clustering of functional glutamate receptors before and after synaptogenesis in hippocampal neurons,* Journal of neurophysiology **84**, 1573 (2000).

[49] C. Tardin, L. Cognet, C. Bats, B. Lounis, and D. Choquet, *Direct imaging of lateral movements of AMPA receptors inside synapses,* The EMBO Journal **22**, 4656 (2003).

[50] U. Sumita, *On conditional passage time structure of birth-death processes,* Journal of applied probability **21**, 10 (1984).

[51] K. Miermans, R. Kusters, C. Storm, and C. Hoogenraad, *Actin remodeling and polymerization forces control dendritic spine morphology,* arXiv preprint arXiv:1510.08816 (2015).

[52] J. A. Cottrell, T. J. Hughes, and Y. Bazilevs, *Isogeometric analysis: toward integration of CAD and FEA,* (John Wiley & Sons, 2009) Book section 2.